Nanoscale Res Lett (2006) 1:99–119
DOI 10.1007/s11671-006-9016-6

NANO REVIEW

Developing 1D nanostructure arrays for future nanophotonics

Harry E. Ruda · John C. Polanyi · Jody (S. Y.) Yang · Zhanghua Wu · Usha Philipose · Tao Xu · Susan Yang · K. L. Kavanagh · J. Q. Liu · L. Yang · Y. Wang · Kevin Robbie · J. Yang · K. Kaminska · D. G. Cooke · F. A. Hegmann · A. J. Budz · H. K. Haugen

Published online: 26 August 2006
© to the authors 2006

Abstract There is intense and growing interest in one-dimensional (1-D) nanostructures from the perspective of their synthesis and unique properties, especially with respect to their excellent optical response and an ability to form heterostructures. This review discusses alternative approaches to preparation and organization of such structures, and their potential properties. In particular, molecular-scale printing is highlighted as a method for creating organized pre-cursor structure for locating nanowires, as well as vapor–liquid–solid (VLS) templated growth using nano-channel alumina (NCA), and deposition of 1-D structures with glancing angle deposition (GLAD). As regards novel optical properties, we discuss as an example, finite size photonic crystal cavity structures formed from such nanostructure arrays possessing high Q and small mode volume, and being ideal for developing future nanolasers.

Keywords Nanostructures · Nanophotonics · Vapour–liquid–solid (VLS) growth · Glancing angle deposition · Molecular scale imprinting · Nanowire photonic crystals

H. E. Ruda (✉) · Z. Wu · U. Philipose · T. Xu · S. Yang
Centre for Nanotechnology, University of Toronto, Toronto, Ontario, Canada, M5S 3E4
e-mail: ruda@ecf.utoronto.ca

J. C. Polanyi · Jody (S. Y.) Yang
Department of Chemistry, University of Toronto, Toronto, Ontario, Canada, M5S 3H6

K. L. Kavanagh · J. Q. Liu · L. Yang · Y. Wang
Department of Physics, Simon Fraser University, Burnaby, British Columbia, Canada, V5A 1S6

K. Robbie · J. Yang · K. Kaminska
Department of Physics, Queen's University, Kingston, Ontario, Canada, K7L 3N6

D. G. Cooke · F. A. Hegmann
Department of Physics, University of Alberta, Edmonton, Alberta, Canada, T6G 2J1

A. J. Budz · H. K. Haugen
Department of Engineering Physics, McMaster University, Hamilton, Ontario, Canada, L8S 4M1

H. K. Haugen
Department of Physics and Astronomy, McMaster University, Hamilton, Ontario, Canada, L8S 4M1

Introduction

Demands for high speed, highly integrated, low power, and low cost electronic and optoelectronic devices continue to drive the development of devices below about 100 nm. Increasingly, the classical semiconductor physics is becoming inadequate as quantum mechanical effects dominate the properties of devices. In this regime, energy states of carriers change from continuous states to quantized discrete states with coincident changes in the density of states (DOS). As a result, novel devices based on the unique novel properties of nanowires can be obtained, such as (1) single-electron transistors, (2) nanowire lasers with lower threshold currents, higher characteristic temperatures and higher modulation bandwidths, and (3) high performance nanowire photodetectors. At the same time, these structures when organized into arrays can offer systems with unique properties. This review is focused on how to realize such advanced structures addressing novel approaches to organization such as molecular-scale

imprinting (MSI), and to synthesis, such as vapor–liquid–solid (VLS) growth and glancing angle deposition (GLAD), leading to a discussion of the particular properties of one-dimensional (1-D) systems. We also discuss how regular arrays of 1-D systems can offer unique opportunities in their properties such as for nanowire array laser photonic cavities.

Section 2 is concerned with MSI as a means of prepatterning surfaces using a two step process of self-assembly and then imprinting. Organized patterns on the atomic scale may be formed by this approach, and are suitable as precursors for subsequent formation of 1-D nanostructures. For example, in Sect. 3 a review of nanowire synthesis techniques are discussed including VLS growth—this technique relies on the presence of catalyst material for growth to occur, with the nanowire dimensions dictated by the size of the initial catalyst deposit. MSI provides a means for atomically defining the location and in-principle size of the deposits, and therefore is the ideal first step in forming organized systems of nanowires. Section 4 discusses the unique properties of nanowires and systems of nanowires, with a strong emphasis on nanophotonics and photonic devices. The paper ends with some broad conclusions in Sect. 5.

Molecular-scale imprinting

It is widely recognized that the fabrication of nanostructures atom-by-atom is a process so slow as to be impractical as a means for manufacturing nanoscale devices. To construct even an object of a few million atoms, it will be necessary to assemble them concurrently, not consecutively. To this end, extensive research has been performed, in many laboratories on ‘‘self-assembly’’. Increasingly, it is becoming possible to self-assemble nanostructures that offer potential use as devices. There is, however, a significant obstacle along this path to device fabrication—namely, that the requirement for self-assembly is very different from that for device-utilization. Self-assembly requires mobility, whereas device-utilization requires stability.

Typically self-assembly occurs at a surface, in the physisorbed state. The subsequent stage of device-utilization customarily involves charge-transfer (CT) to the self-assembled structure or current flow through it. However, with each attachment or detachment of an electron or a hole, the interaction between the nanostructure and its underlying substrate alters markedly, thereby tending to shake the structure loose from its weak physisorption moorings. It would appear, therefore, that successful device fabrication will involve two consecutive stages; the mobile stage of self-assembly and a subsequent stage of immobilization that we refer to as ‘‘imprinting’’. Crucial to the imprinting stage—as also in any macroscopic printing process—is pattern-retention in going from the ‘‘type’’ to the ‘‘imprint’’. The printing process may be seen as an induced chemical reaction in which the physisorbed structure is converted to the chemisorbed state. Since self-assembly, which is a process of diffusion, takes a finite time, t_{sa}, it is advantageous to be able to select t_{sa}, and subsequently induce the imprinting reaction (physisorption $\rightarrow$ chemisorption) at a chosen instant, t_{imp}, by means of a brief pulse of energy delivered in the form of heat, light or incident electrons.

The requirement that the pattern which constitutes the physisorbed nanostructure shall print—i.e., chemically react—with the underlying surface without alteration in pattern, can readily be translated into the language of ‘‘reaction dynamics’’. Reaction dynamics is the study of atomic and molecular motions in chemical reactions. The requirement that a physisorbed pattern print unaltered as a chemisorbed one is, therefore, a requirement for fully localized reaction at the atomic level. ‘‘Chemical reaction’’ consists in the transfer of all or part of the physisorbed molecule, previously loosely attached by physisorption to the surface, and therefore at a distance from it, downward to the more-strongly covalently bound separation from the surface. In a well-localized reaction this transfer from the physisorbed to the chemisorbed state occurs without lateral displacement across the surface by so much as one atomic spacing. Only then is the molecular-scale pattern fully retained.

A priori one might suppose that the requirements for highly localized reaction would be stringent, including (a) a reaction coordinate (direction of approach of the reagents) which is normal to the surface-plane, and (b) minimum possible translational energy along the reaction co-ordinate. Conditions (a) and (b) would make it likely that the atom or group approaching the surface had only a negligible momentum across the surface, thereby tending to suppress reaction at a distance from the original point of impact.

In fact the first example of the fully localized ‘‘imprinting’’ of a physisorbed nanostructure as an indistinguishable chemisorbed atomic pattern [1] is unlikely to have satisfied either criterion (a) or (b) above. It would appear, therefore, that ‘‘molecular-scale imprinting’’ (MSI) and its accompanying highly localized reaction does not make such stringent requirements on the molecular dynamics; the approach to the surface need not be strictly at 90° to the surface-plane, nor need the reaction be induced at its threshold

energy. This is, of course, favorable to the prospects for generalizing the method of MSI. This is not to say that any physisorbed nanostructure will chemically imprint its pattern in unaltered form. It seems probable, however, that a broad category of reagents will do so, under achievable experimental conditions.

Reference 1 provides an example of a physisorbed self-assembled pattern of methyl bromide, CH_3Br(ad), adsorbed at approximately 50 K surface-temperature at a Si(111) 7 × 7 surface. Figure 1a shows an STM image of the clean surface at V_s = 1.5 V, Fig. 1b shows the circles of physisorbed CH_3Br(ad) found at 50 K, and Fig. 1c shows a close-up of one of these circles comprising 12 well-separated CH_3Br(ad) molecules. This is the molecular ''type'' prior to imprinting. Though not previously reported for CH_3Br(ad), such rings are well-known for benzene at 78 K [2], which, however, has not been observed to chemically ''imprint''. Figure 1d shows the effect of 193 nm radiation on CH_3Br(ad) at the unchanged surface voltage of V_s = 1.5 V; the bright physisorbed circles of CH_3Br(ad) have disappeared leaving dark circles of

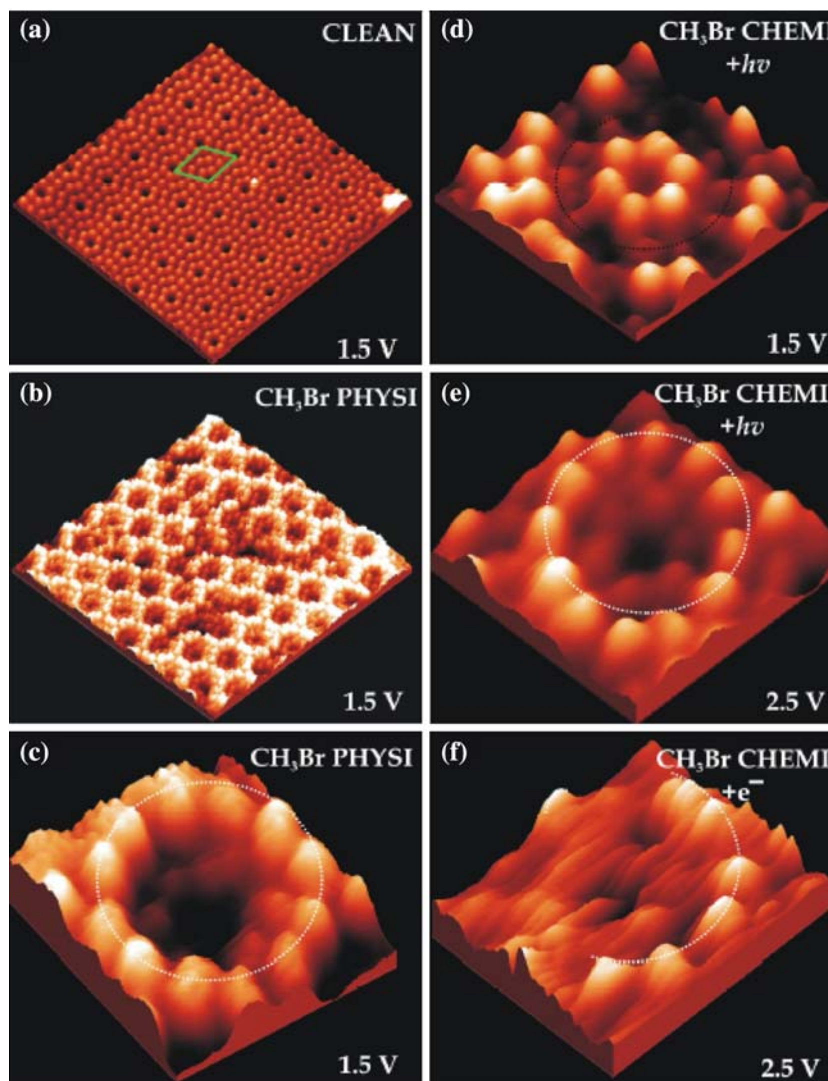

Fig. 1 (**a**) STM image of the clean Si(111)7 × 7 surface at 50 K. A 7 × 7 unit cell is indicated. $V_{surface}$ = 1.5 V, current = 0.2 nA, ~20 × 20 nm. (**b**) STM image of physisorbed CH_3Br(ad) on the 50 K Si(111)7 × 7 surface at a coverage of 0.41 monolayer. Physisorbed molecules appear as protrusions over the middle adatoms. $V_{surface}$ = 1.5 V, current = 0.2 nA, ~20 × 20 nm. (**c**) Zoomed-in STM image of a single ring of physisorbed CH_3Br on Si(111) surface (indicated by the dotted circle), as in (**b**) but ~30 × 30 Å. (**d**) Chemisorbed Br on Si(111) surface after photolysis of (three successive applications of) physisorbed CH_3Br(ad) at 50 K. Br (beneath dotted circle) appears as depressions on the middle adatoms. $V_{surface}$ = 1.5 V current = 0.2 nA, ~30 × 30 Å. (**e**) STM image of chemisorbed Br imprints on the middle adatoms (indicated by a dotted circle) as in (**d**) but with $V_{surface}$ = 2.5 V. (**f**) STM image of chemisorbed Br on the middle adatoms (dotted-in) obtained by scanning (a single application of) physisorbed CH_3Br(ad) at 2.5 V (scans from lower left to upper right); $V_{surface}$ = 2.5 V, current = 0.2 nA, ~30 × 30 Å

Br–Si which, in Fig. 1e, 'light up' to give 12 bright Br–Si at $V_s = 2.5$ V. This is the well-known voltage-dependence of Br–Si STM images [3].

Definitive proof that the physisorbed CH_3Br(ad), only observable at the surface ≤50 K, had been converted to a chemisorbed species was to be found in the fact that the circular patterns of Fig. 1e following UV irradiation survived unaltered when heated to 200°C for over 1 min. Undoubtedly, chemisorption had occurred. There is no way, however, that intact CH_3Br(ad) could become strongly chemisorbed at the surface, but there is abundant evidence that physisorbed methyl halides undergo photoreaction to halogenate reactive substrates [4–10]. What is new is the identification, by STM, of this photoreaction as being a *highly localized event*; i.e., Br–Si forms exclusively at the Si-atoms directly beneath the parent CH_3Br(ad) molecules.

A number of authors have proposed and found evidence that the major cause of photo-induced surface reaction in physisorbed organic halides is charge-transfer from the substrate to the adsorbate [4–10]. Not surprisingly, therefore, the reaction of CH_3Br(ad) with Si(111) 7×7 could be induced by electrons of sufficient voltage coming from the STM tip (namely 2.5 V). Figure 1f shows that the reaction induced in this fashion is, as before, highly localized, giving rise to rings of chemisorbed Br–Si in place of the original rings of physisorbed CH_3Br(ad).

Figure 2 gives a schematic representation of the process of MSI. A circle of 12 physisorbed CH_3Br(ad) are shown in Fig. 2a. In Fig. 2b, following irradiation by photons or electrons the Br (red) are shown reacting locally to brominate only the Si-atoms beneath the CH_3Br(ad). The CH_3(g) radicals are thought to leave the surface, since the characteristic black features indicative of methyl bound to silicon were not observed in the STM images following irradiation.

It remains to explain the highly localized nature of the observed reaction. Figure 3 is the physisorption geometry of CH_3Br(ad)/Si(111) 7×7 computed in the MP2 approximation. As expected the most-stable configuration is that with the Br-end of CH_3Br pointing downward toward the Si surface. However, the C–Br bond is found to be at an angle of approximately 60° to the surface normal. When, therefore, an electron is transferred to the CH_3Br^- anti-bonding orbital, causing the C–Br bond in CH_3Br^- to extend, the Br is expected to hit the surface at an angle to the surface-plane (cf. condition (a) of the previous discussion). Since the photon energy at 193 nm is 6.3 eV, the photo-electron will bring several eV of excess energy to the CH_3Br (cf. condition (b); previous discussion). A priori one might expect, therefore, that there would be substantial migration of Br across the surface with a resultant "blurring" of the Br–Si imprint as compared with the parent CH_3Br(ad) pattern. This is not, however, observed.

From a fundamental standpoint, the observation of highly localized reaction under conditions that seem to strongly favor de-localization is an interesting conundrum. The proposed explanation [1] is that the Br^- from CH_3Br recoiling toward the surface (even though at a glancing angle of incidence) rides up a repulsive wall and spends ~10^{-13} s at the repulsive turning-point before recoiling. These 100 fs are long enough to permit

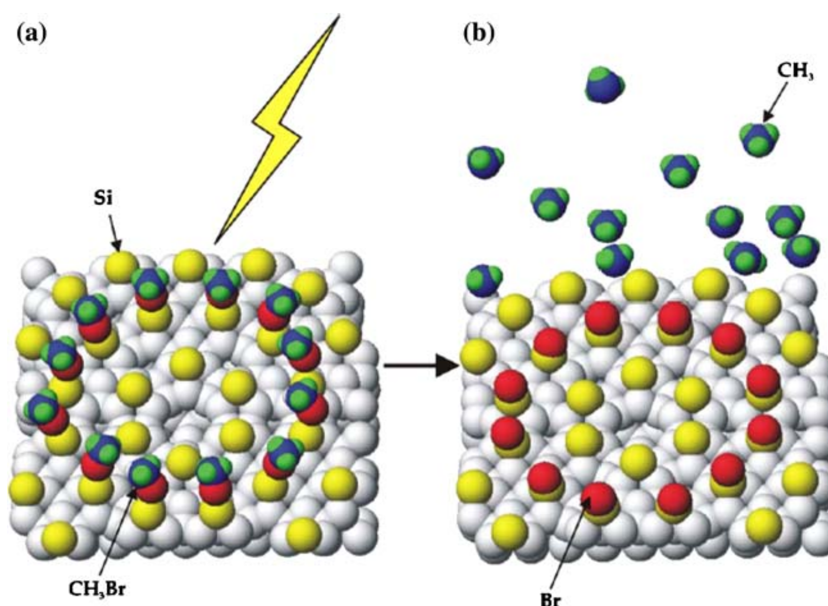

Fig. 2 Schematic representation of (**a**) physisorption of CH_3Br on Si(111) surface with Br pointing down, and (**b**) chemisorbed Br on middle adatom positions, after photolysis or electron-impact at 50 K

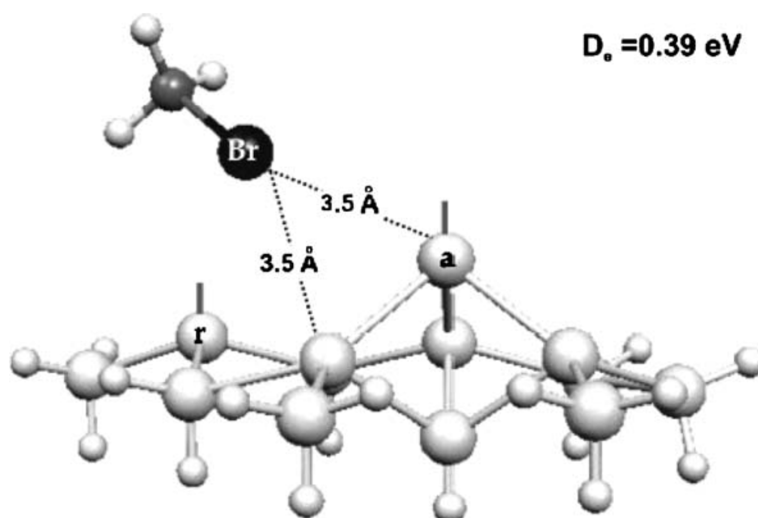

Fig. 3 A depiction of the equilibrium physisorption geometry for CH_3Br, showing C–Br lying at an angle of ~60° to the surface normal. The cluster is $Si_{13}H_{18}$ distributed in three layers (a = adatom, r = rest atom)

reverse charge-transfer to take place from Br^- to the underlying silicon surface [11], with the result that Br^- is trapped in the potential-well of the first Si atom that it encounters, i.e., the reaction is highly localized.

The proposed mechanism for MSI [1] is illustrated in Fig. 4 as a three-stage process. The energies are calculated by density functional theory (DFT) for the simple model of (1) charge-transfer to the methyl bromide from the silicon surface, $CH_3Br + e^- \rightarrow CH_3Br^-$, (2) transfer of Br^- from methyl bromide to the surface modeled as $CH_3Br^- + SiH_3 \rightarrow CH_3 + Br^- \cdot SiH_3$, followed by (3) charge-transfer in ~10^{-13} s. back to the silicon surface, $Br^- \cdot SiH_3 \rightarrow Br–SiH_3 + e^-$. The three consecutive stages are indicated by the three arrows labeled (1), (2) and (3) in the figure. It is evident that the loss of energy to the surface in stage (3) transfers Br from the repulsive $Br^- \cdot SiH_3$ state to the bound $Br–SiH_3$ state, in which it is held captive by a strong covalent bond. Localized reaction, and hence MSI, has taken place.

Nanowire synthesis

Growth on vicinal substrates

Several groups have reported on the growth of self-assembled nanowires on vicinal substrates [12–20]. Figure 5 illustrates the process of nanowires growth on vicinal substrates. The substrates are miscut with an angle of 1–50°. Materials are alternatively deposited on the substrates. The expitaxial growth for two materials is performed in A layer-by-layer or step-flow growth mode. The growth starts at the step edges and causes lateral composition modulation. The tilt angle of the nanowires is sensitive to the coverage of each

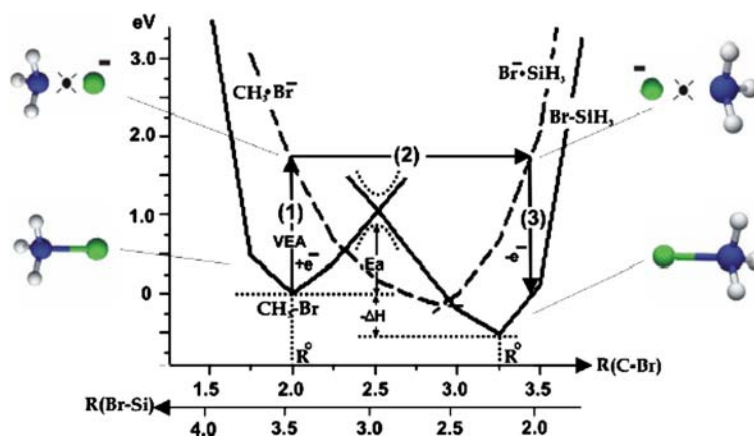

Fig. 4 Simple density functional theory (DFT) ab initio model of the charge-transfer (CT) reaction with co-linear C–Br–Si: (1) $CH_3Br(ad)+e^-$ gives $CH_3 \cdot Br^-$, (2) $CH_3 \cdot Br^-$ gives $Br^- \cdot SiH_3$, and (3) $Br^- \cdot SiH_3$ gives $Br–SiH_3+e^-$. The dots indicate repulsion. Repulsion in step 2 was calculated separately for $CH_3 \cdot Br^-$ and $Br^- \cdot SiH_3$. VEA = vertical electron affinity; E_a = activation energy; $-\Delta H$ = heat of reaction

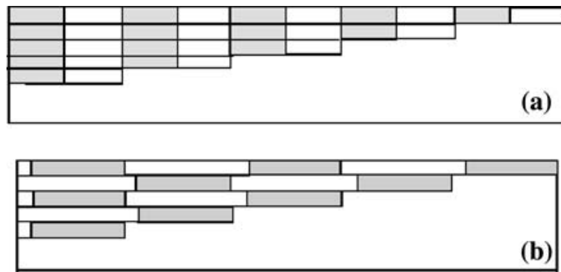

Fig. 5 Schematic illustration of nanowire grown on a vicinal substrate

deposition cycle. If a total of one monolayer per cycle is deposited, the nanowires are formed perpendicular to the terraces. The nanowires tilt to the steps if less than one monolayer per cycle is deposited. But if more than one monolayer per cycle is deposited, the nanowires tilt away from the steps. Serpentine superlattice nanowires can also be formed on the substrate by this method by sweeping the per-cycle coverage through a range that is needed for a vertical structure [14].

Growth on high-index substrates

Nanowires have been demonstrated to grow on high-index substrates [21, 22]. Nötzel et al. have reported on growth of GaAs nanowires on high-index surfaces of GaAs (311)A [21]. The growth of nanowires on high-index surfaces is due to formation of an array of nanometer-scale macrosteps or facets with a periodicity determined by energy rather than growth-related parameters. The layer-by-layer growth of flat surface having high surface free energy is broken up by forming facets with lower surface free energy to minimize the surface energy, resulting in the formation of macrosteps. Macrosteps oriented along the [233] direction on the GaAs (311)A are formed by two sets of {331} facets having roughly half the surface free energy. The complete structure containing alternating thicker and thinner channels of GaAs and AlAs forms the nanowires oriented along [233] direction.

Self-assembled Ge nanowires have also been reported to grow on high-index Si (113) substrates [22]. The nanowires do not orient along steps, instead they orient along [332] direction and perpendicular to the steps. It is believed that the orientation of elongated anisotropically strained Ge islands are energetically favored in the [332] direction.

Grown on V-grooved substrates

Growth of nanowires can be realized on non-planar substrates, or so-called V-grooved substrates [23–31]. Different facets are formed on such substrates. The migration of adatoms and effective sticking coefficient associated with different facets are different. These phenomena results in different growth rate on the different facets, and thus results in lateral thickness modulation across the substrate structure. V-grooves are typically fabricated on GaAs (100) using electron-beam or optical lithography and wet etching, and are oriented along [01 $\bar{1}$] direction. Preferential growth of GaAs on the (100) surfaces located at the bottom of the V-grooves, results in the formation of crescent-shaped nanowires. Nanowires have also been grown on patterned high-index GaAs (n11) substrates [32]. This is realized by selective growth on the sidewall on one side of the mesa top and oriented along the [01 $\bar{1}$] direction. The fast growth on the side walls results from the preferential migration of Ga atoms from the mesa tops and bottoms toward the sidewalls.

Glancing angle deposition

Aggregation of atomic vapors onto flat surfaces can produce morphological structures with a surprising degree of complexity and, to some degree, self-organization. Inter-atomic competition for preferred incorporation sites in a growing thin film, when coupled with dynamic variation of substrate orientation, creates a growth regime that is both fundamentally unpredictable and potentially technologically useful [33, 34]. By choosing growth parameters, such as temperature, deposition rate, film material, and substrate orientation, atomically-structured porous materials can be synthesized with novel functional response characteristics. These techniques have been demonstrated to allow fabrication of single-material optical interference coatings [35], broadband antireflection coatings [36], and other photonic crystals [37, 38]. While fractal scaling effects have been found to limit the utility of these films for some applications [39, 40], these atomic-scale architectures appear to be uniquely functional three-dimensional (3-D) organized materials [41–44].

Most thin film deposition technologies attempt to produce fully dense or crystalline coatings. When conducted under conditions that prevent film densification (low temperature, high deposition rate, etc.), thin film growth allows the fabrication of a wide variety of atomically porous structures, whose electromagnetic, biological, etc. response depends strongly on the morphology. Figure 6 illustrates the difference between conventional thin film crystal growth (a, b1, c1, d1) versus atomically porous growth (a, b2, c2, d2) where atomic vacancies are “frozen in” to the film

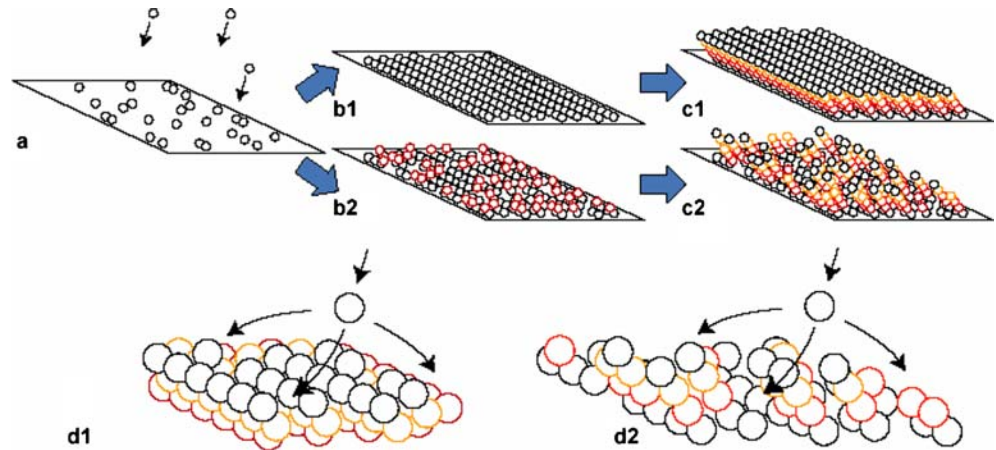

Fig. 6 Schematic illustration of atomic aggregation: growth of fully dense crystals (a, b1, c2, d1), and transport-limited growth of atomically structured porous thin film coating (a, b2, c2, d2)

structure. When atoms condensing from the vapor (a) are able to fill all crystal sites (b1), the resulting coating is fully dense and crystalline (c1). If the condensing atoms are prevented from filling crystal sites (b2), by transport limitations during ballistic transport or surface diffusion, the resulting coating is atomically porous (c2). At each stage of growth the difference is as illustrated in (d1 and d2) where in (d1) each arriving atom is able to reach and condense in a vacant lattice site, whereas in (d2) arriving atoms are unable to fill each possible site. Exploiting this atomic-scale competition effect, GLAD, Fig. 7, employs dynamic substrate motion during growth to shape deposited thin film coating structures. Atoms, evaporated from a bulk quantity of the source material, sequentially arrive at the substrate by ballistic transport, and condense to form a thin film coating. The large substrate tilt enhances inter-atomic shadowing, producing porous coatings with structures that can be controlled by specifying the substrate orientation, including dynamically [45]. The cross-section of a silicon thin film deposited in this way is shown in Fig. 7b, where rod-like morphological structure is seen to grow perpendicular to the substrate, with characteristic dimensions of tens of nanometers. Given the nearest-neighbor spacing in crystalline or amorphous silicon of approximately 250 pm, the 100 nm scale bar shown corresponds to the linear dimension of about 400 atoms. Fine structure within the silicon rods is observable down to the resolution limit of the scanning electron microscope at approximately 5 nm, or about 20 atoms.

Because the thin film coatings produced with GLAD are atomically porous, their electromagnetic response is best described with effective medium theory, which predicts an effective response that to first order is a density-weighted sum of the response of the film material and the void regions [46]. Using this knowledge, single-material periodically in-homogenous coatings were produced to demonstrate 1-D optical interference effects, including so-called Rugate filters with sinusoidally varying refractive index [35]. If the

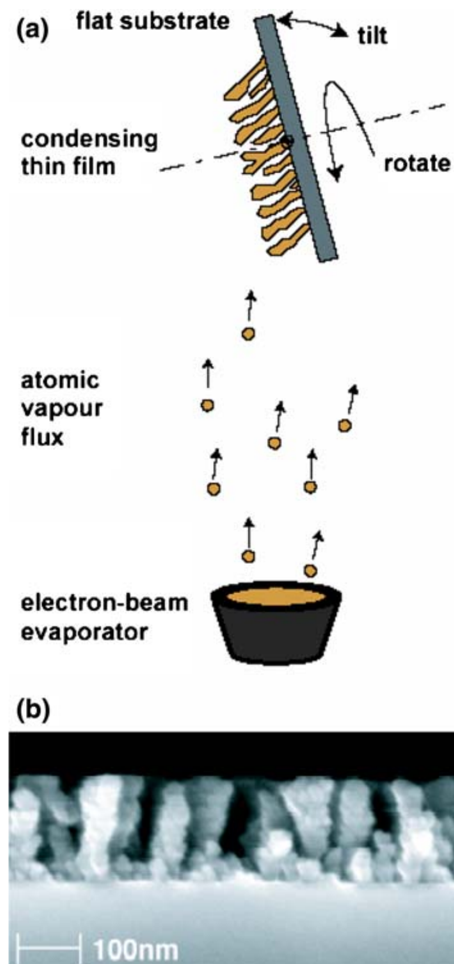

Fig. 7 (**a**) Schematic illustration of glancing angle deposition (GLAD), employing substrate tilt and rotation relative to the condensing atomic vapor flux to create atomically engineered coatings. (**b**) Scanning electron micrograph fracture cross-section of a silicon thin film deposited onto a rapidly rotating substrate at 85° tilt

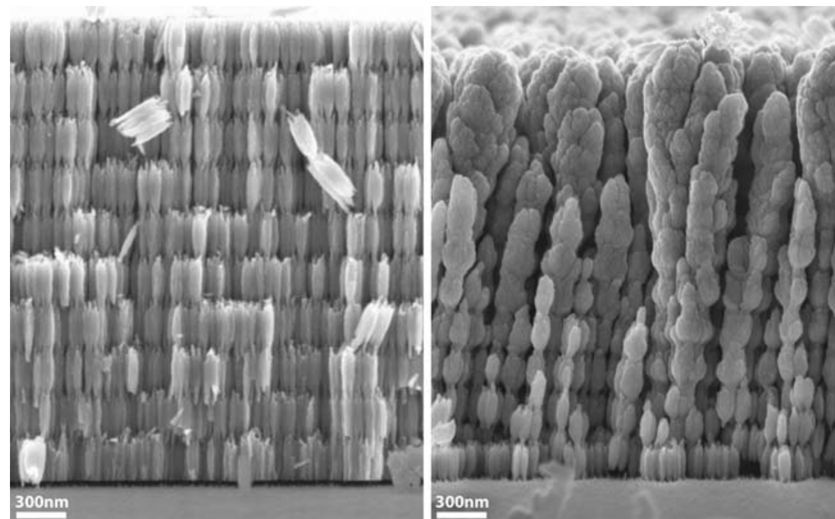

Fig. 8 Scanning electron micrograph fracture cross-sections of periodically inhomogeneous optical interference filters, fabricated from silicon, showing (**a**) stable growth, and (**b**) fractal scaling during growth

porosity of the most-porous layers within the structure is kept intentionally low (by limiting the substrate tilt to approximately 80°), a repeating structure is produced (Fig. 8a) with a strong optical stop-band, as predicted by theory. If, however, highly porous layers are included in the filter design (by tilting the substrate beyond approximately 80°), a morphological scaling effect is seen (Fig. 8b) that transforms the growing interface from two dimensions to a fractal 2+ dimension. This result is explained by chaotic growth mechanics that are intrinsic to film deposition at these glancing deposition angles, and produce power-law scaling in the morphological structure [39, 40, 46, 47]. While these scaling effects do place constraints on what morphological structures are possible with this technique, they also provide unique benefits. Figure 9 displays a silicon optical filter, where the bifurcating chaos of glancing deposition is exploited to produce an antireflection coating that is continuously graded in porosity to yield an effective refractive index of 1.0 at the surface—a theoretically ideal index match to air or vacuum ambient. By continuously, and controllably, increasing the substrate tilt to 90°, a 5th order polynomial (or quintic) decrease in refractive index was accomplished, yielding a highly effective broadband infrared antireflection coating [36]. Experimental results are in good agreement with theory, suggesting that this type of coating might be suitable for coatings on high power laser optics, low-loss optical communication components, and others.

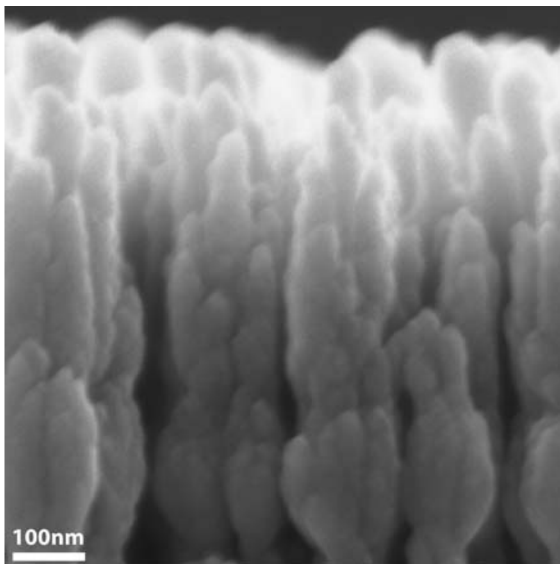

Fig. 9 Scanning electron micrograph fracture cross-sections of a quintic broadband antireflection coating where porosity and effective refractive index are continuously graded to match the air/vacuum ambient

A recent advance in nanostructured thin film coatings is the development of shaped nano-particles that are fabricated as constituents of a thin film, then removed from their substrate to produce a collection of loose nano-particles, or a nano-powder. Figure 10 shows scanning electron micrographs of these particles. The particles, in this case composed of silicon, are helicoidal and about 1 μm long and 200 nm in diameter. The helical pitch is approximately 200 nm. They are fabricated by: depositing a dense sacrificial layer on a substrate (in this case NaCl—table salt), depositing the film with controlled substrate motion (in this case silicon deposited onto a slowly rotating substrate held at a fixed tilt angle of 85°), dissolution of the sacrificial layer in water creating a suspension of the particles in saltwater, successive dilution and centrifugation to remove the salt and produce a suspension of the

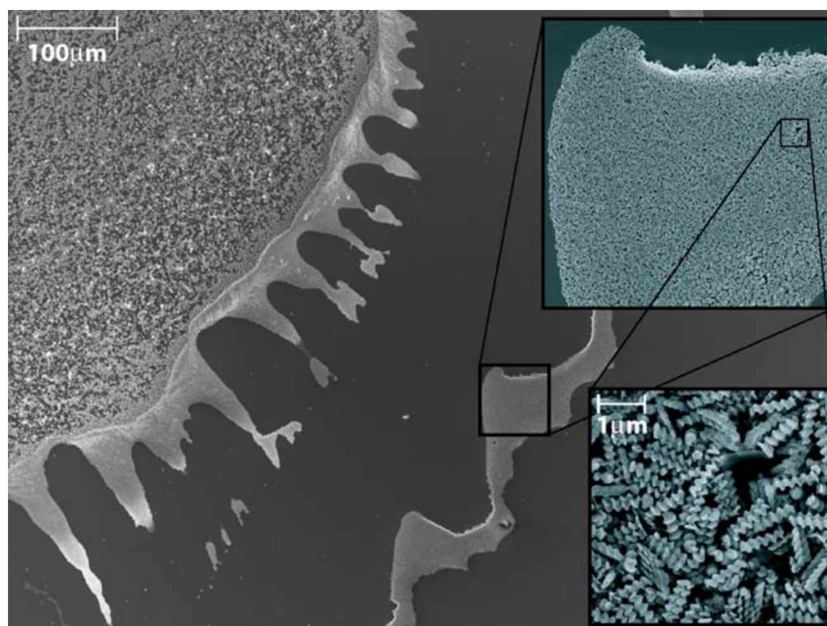

Fig. 10 Scanning electron micrograph plan-views of synthesized chiral silicon nano-particles, displaying drying-drop pattern formation (main image), and aggregated loose nano-particles (two insets)

particles in pure water. To image the particles with scanning electron microscopy, a drop of the final suspension was placed on a flat silicon substrate, and the water was allowed to evaporate, leaving the drying ring and nano-particles seen in Fig. 10. The particles can be individually separated by dilution, and their structure can be specified by designing the substrate motion during growth (for example right-handed helices are produced by rotating the substrate one direction during growth, left-handed by rotating the opposite). Figure 11 shows helicoidal (a) and rod-like (b) silicon nano-particles. The size, and controlled morphology, of these nano-particles suggest they might be useful in experiments probing biological function, particularly as they have an optical response that can be tailored, and could be made to exhibit a signature response that would allow accurate location of perhaps individual particles. Preliminary experiments have shown that the chiral structure of the helicoidal particles in suspension results in circular polarization effects or ''optical activity'' [42] including circular dichroism where the periodic structure of the helix produces a resonance condition for light matching the pitch and handedness of the structure. By choosing growth conditions (substrate rotation rate or rotation direction) specific optical response characteristics can be engineered. These particles can also be treated as nanophotonic components in a larger system, and might be useful in self-organized architectures for advanced sensing, communication, or computation applications.

VLS growth

Free standing nanowires can not be obtained using above mentioned methods. A more general method to synthesize virtually any semiconductor nanowires is

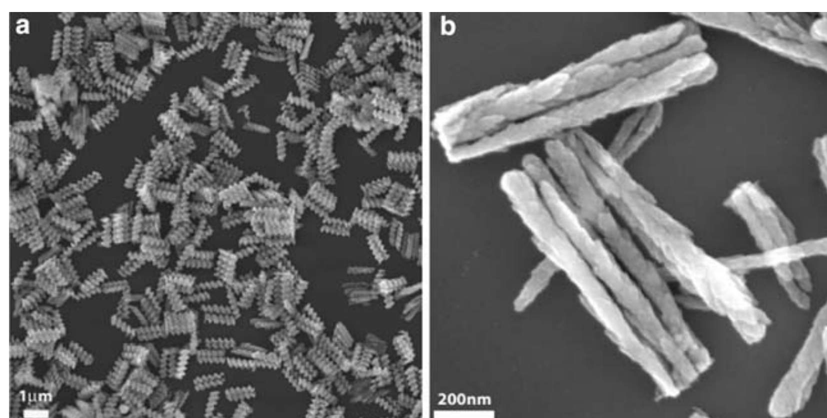

Fig. 11 Scanning electron micrograph plan-views of synthesized silicon nano-particles, illustrating (**a**) helicoidal, and (**b**) rod-like, morphologies

based on VLS growth mechanism. VLS growth was first introduced in 1964 by Wagner and Ellis [48]. A naturally occurring terrestrial example of VLS growth is that of Germanium Sulfide whiskers, observed in condensates of gases released by burning coal in culm banks by Finkelman et al. [49].

Generally, metal is used as the liquid-forming agent. The metal forms droplets of a liquid alloy with the grown and/or solid substrate. The droplets dissolve material from the vapor phase. These materials diffuse to the liquid–solid interface and precipitate out to form nanowires or whiskers. The kinetics and mechanism of VLS growth has been studied in detail by Givargizov [50].

Review of different approaches to VLS growth

There are a number of approaches reported for VLS growth of nanowires or whiskers. Chemical vapor deposition (CVD) has been mainly used for VLS growth of whiskers in its early stage of investigation mainly focused on Si and Ge at high growth temperature ranging from 950 to 1200°C and using Au, Pt, and Au–Pt alloy as liquid forming agents [51–55]. At such high growth temperature, the diameter of whiskers range from 1 to 140 μm.

Ruda et al. have reported on growth of Si nanowires using VLS-CVD using Au as the mediating solvent at low temperature from 320 to 600°C [56]. It has been shown that Si nanowires with diameter as small as 10 nm can be grown at low temperature and high partial pressure.

Hiruma et al. [57–59] have grown III–V group semiconductor whiskers such as GaAs and InAs using metalorganic CVD (MOCVD) based on VLS mechanism and using Au as catalyst at growth temperature of 450–500°C. It has been found that the whiskers grown using CVD [60] and MOCVD [57, 58] are tapered, this is because of the high lateral growth on the sidewall of the whiskers due to the high pressure growth conditions.

Lieber et al. [61–64] extended the VLS growth mechanism for nanowire growth of a broad range of semiconductors including III–V and II–VI groups using laser ablation. Using this method, nanowires with diameter as small as 3 nm can be obtained. There is also no tapering effect in the nanowires. Since a target containing both the growth material and the metal for catalyst agent is used, precision control of length and composition of compound semiconductors, particularly those with more than two elements, becomes difficult.

Ruda et al. [65, 66] have reported on VLS growth of semiconductor nanowires using MBE in ultra-high vacuum conditions. In VLS-MBE approach, the lateral growth of nanowires is dramatically suppressed because of the limited availability of source materials on the side walls due to the strong directionality of the source beams of MBE. Figure 12 shows condensed and well-oriented GaAs nanowires grown on GaAs (100) substrates. It has been shown that the nanowires are single crystal with homogenous diameter along wire axis as shown in Fig. 13. Most of the VLS-grown nanowires grow along < 111 > direction. It has also been shown that a small percentage of defect-free nanowires grow along < 110 > direction.

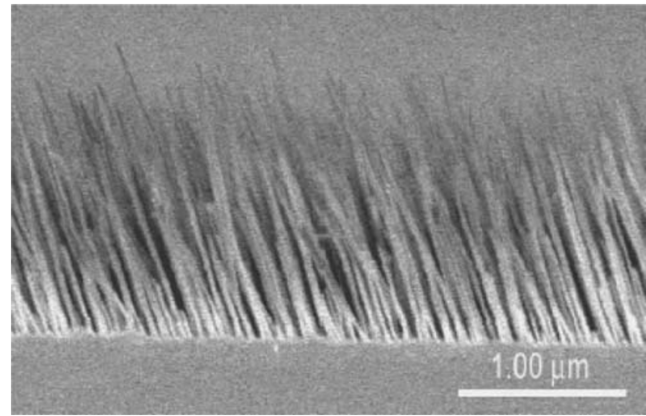

Fig. 12 A scanning electron microscope image of GaAs nanowires grown on a (001) GaAs substrate

Diameter and site control

Control of nanowire diameter is an important issue. There are three factors can be used to control the diameter, namely, growth temperature, vapor–solid deposition rate which also depends on the growth temperature, and size of catalyst particles. For a given size of catalyst particle, the volume of the droplet of liquid alloy is given by the phase diagram. More materials can be dissolved in the droplet at a higher temperature. This results in bigger droplets and therefore larger diameter nanowires. Higher vapor–solid deposition rate results in higher lateral growth rate on sidewalls of the nanowires and thus larger diameter nanowires. This is particularly serious for CVD and MOCVD growth of nanowires because of the inherent high growth pressure conditions. For a given temperature, smaller sized particles give smaller droplets and thus smaller nanowire diameters. Indeed, this is part of the current motivation for studies of MSI as a means of patterning nanoscale droplets—see Sect. 2 for more details on this technique.

Diameter-controlled synthesis of Si nanowires has been demonstrated by depositing well-defined Au nanoclusters on Si substrates using CVD growth [67].

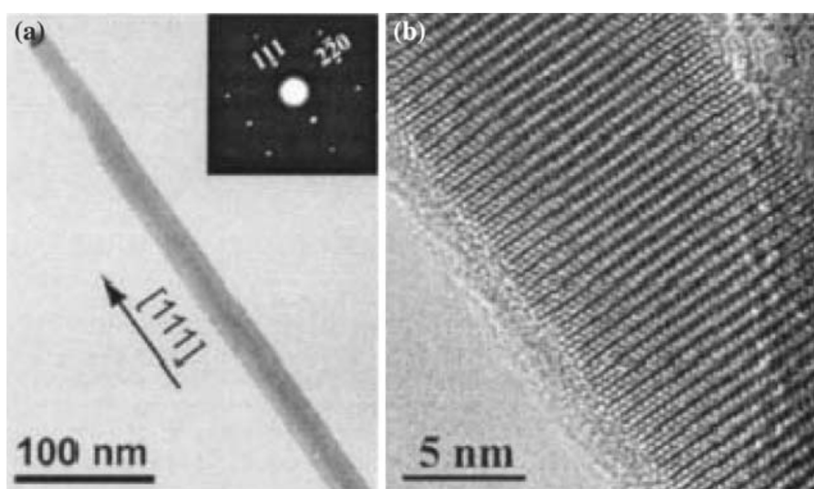

Fig. 13 Low magnification (**a**) and high resolution (**b**) transmission electron microscope images of a GaAs nanowire

A clear correlation between the size of Au nanoclusters and the size of resulting Si nanowires has been found. The disparity of Si nanowires is limited only by the dispersity of Au nanoclusters. Ohlsson et al. [60] demonstrated another method for synthesis of size-controlled GaAs nanowires by depositing size-selected gold aerosol particles on a GaAs (111)B substrate using CVD. The Au particles are created by evaporation or condensation method and charged by UV light. The particles are size selected by a differential mobility analyzer, which classifies the sizes of charged aerosol particles by balancing their air resistance against their mobility in an electric field. Shimada et al. [68] have demonstrated the control of the size of nanowhiskers by artificially changing the Au droplet size by tuning the Au deposition. The minimum diameter can be as small as 10 nm by reducing the Au deposition, however, the density of Au droplets also decreases. Another important issue for nanowire growth is the site controlling. This is necessary for integration of nanowire technology with semiconductor component technology for device applications. Ohlsson et al. have demonstrated site controlled placement of nanowires by manipulating the Au particles on the substrate using atomic force microscopy [69]. Sato et al. [68, 70] have reported the site controlled growth of GaAs whiskers on GaAs substrates by depositing Au through SiO_2 mask window formed by electron-beam lithography. When the window size increases, the number of whiskers grown inside the window increases.

Planar nanowhisker arrays have also been grown using characteristic growth of GaAs nanowires along [111]B direction [71]. The growth starts with creating a step with {111}B sidewall by patterning using photolithography followed by wet etching. SiO_2 is deposited on the substrate except the GaAs step side. Au is deposited on sidewalls of steps without SiO_2 mask. GaAs whiskers are grown on the sidewalls of steps using MOCVD. Growth of lateral nanowire bridging between two parallel sidewalls of steps has also been demonstrated [72].

Site-controlled processing for nanowire growth using AFM or electron beam lithography is, however, high-cost, time-consuming and low-throughput. Ruda and coworkers [65] have demonstrated a method for size- and site-control growth of nanowires. In this method, a nano-channel alumina (NCA) with highly ordered pores is used as a template to define the size and site of Au dots for nanowire growth. Fig. 14 illustrates the process flow for preparing ordered nanowires with a template. Au is deposited through the template. Highly ordered Au dot arrays are obtained on a substrate after etching away the NCA template.

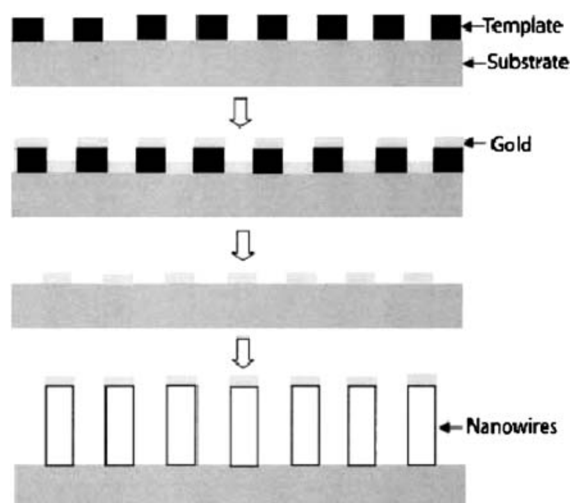

Fig. 14 Schematic illustration of the process flow chart for the preparation of ordered arrays of nanowires using a nano-channel alumina (NCA) template

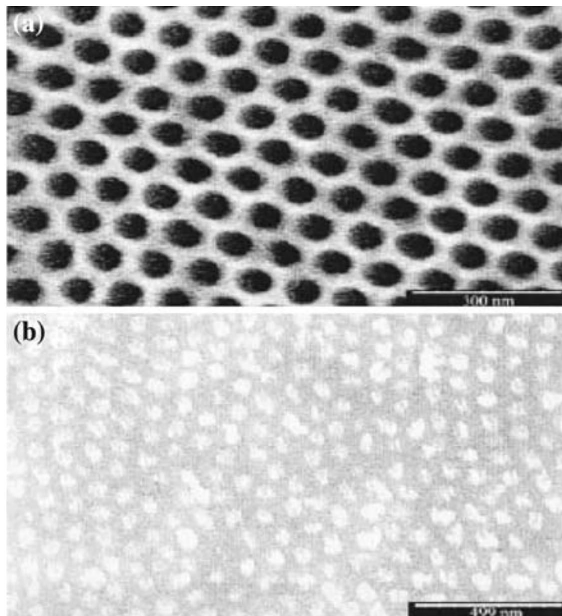

Fig. 15 A plan-view scanning electron microscope image of a nano-channel alumina (NCA) template (**a**) and associated array of gold dots (**b**) formed by evaporation through the template

Figure 15 shows the prepared NCA template and Au dot array deposited through the NCA template.

GaAs nanowires are grown on GaAs substrates with highly ordered Au dot array using MBE. Figure 16 shows FE-SEM images of a highly ordered GaAs nanowire array. The diameter distribution of nanowires grown using NCA template is about three times narrower than that without NCA as shown in Fig. 17. It has been demonstrated that highly ordered nanowire arrays with very narrow size distribution can be grown using NCA templates.

Doping, p–n junctions, heterostructures and superlattices

It is important to use conventional semiconductor technologies such as doping, p–n junction formation, and forming heterostructures and superlattices, to prepare semiconductor nanowire devices. Cui et al. [73] demonstrated the doping of single crystal silicon nanowires using CVD, by incorporating B_2H_6 in the SiH_4 gas stream. Two-terminal, gate dependent electrical measurements showed that the resulting silicon nanowires were p-type. N-type of doping of silicon nanowires was also demonstrated using phosphorus as the dopant. GaAs nanowire p–n junctions have been demonstrated by Haraguchi et al. [74]. N-type doping of ~1×10^{18} cm^{-3} was achieved for GaAs nanowires using MOCVD and using di-silane as the dopant species. Carbon doping was also demonstrated with a

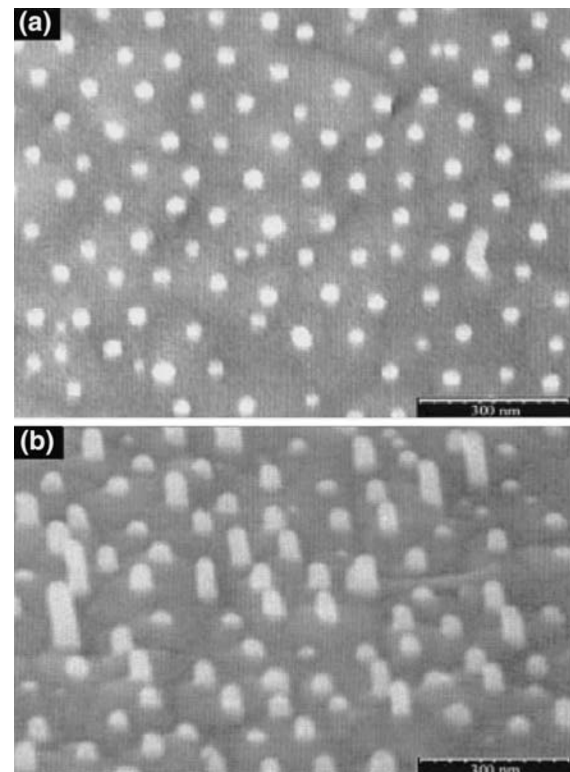

Fig. 16 Scanning electron microscope images of an ordered array of GaAs nanowires in plan view (**a**) and side view (**b**) grown using a nano-channel alumina (NCA) template

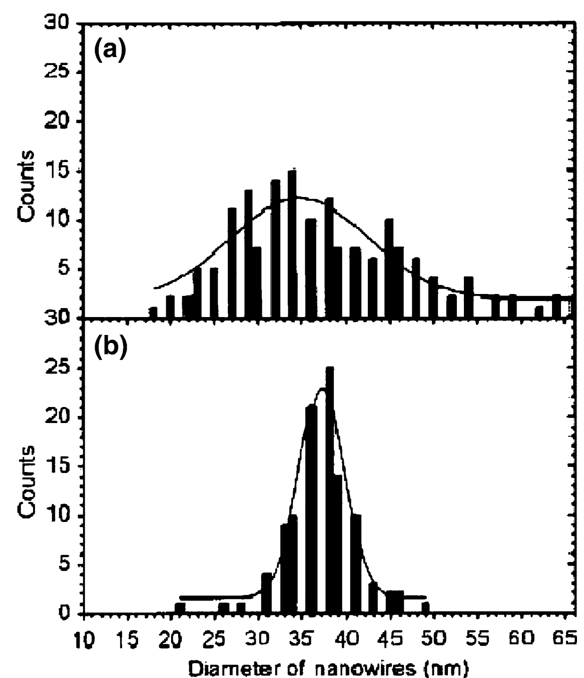

Fig. 17 The diameter distribution of nanowires grown without (**a**) and using a nano-channel alumina (NCA) template (**b**): solid lines are a Gaussian curve fit to the distribution data

p-type doping concentration of ~8×10^{18} cm^{-3}. InAs/InP 1-D heterostructures in nanowhiskers have been grown using CVD by sequential switching of sources followed by a procedure including growth interruption [75]. GaAs/GaP superlattices within nanowires were grown by repeated modulation of vapor-phase reactants during the growth of nanowires, using laser ablation of solid targets [69]. Single crystal Si/SiGe superlattice nanowires have also been grown in a quartz furnace tube using a combination of pulsed laser ablation and CVD [76]. During the growth, a gas mixture of H_2 and $SiCl_4$ was continuously introduced into the reaction tube, while the SiGe alloy layers in the superlattice were obtained by repeated ablation of a Ge target by periodically switching on and off the laser beam.

Beside the heterostructures formed by axial composition modulation, it is also possible to form heterostructures by radial composition modulation. Lauhon and coworkers have reported on the synthesis of Ge/Si core-shell nanowire heterostructures [77]. In their growth, a Si nanowire core was first grown on an oxidized Si substrate in a quartz tube using CVD and silane as the source species. A Ge shell was then deposited upon these nanowires. The radial growth rate for the shell growth was enhanced by placing the growth substrate downstream to favor un-catalysed lateral growth, and where the thermal decomposition of reactants increases as the gas flows through the furnace.

Core-shell heterostructured GaN/ZnO nanowires have also been grown by epitaxial casting of a GaN shell on to a ZnO nanowire core using VLS-CVD growth [78]. Single crystal GaN nanotubes have been formed by subsequently removing the ZnO core nanowire by thermal reduction and evaporation.

Solution phase synthesis

Synthesis from aqueous solution

Vayssieres et al. [79–81] have reported on a method to synthesize nanorods and nanowires from aqueous solutions. This method originated from experimental monitoring of water-oxide interfacial thermodynamics and following nucleation, growth, and aging processes by means of chemical and electrostatic control of the interfacial free energy. The control of interfacial free energy in a system can be achieved by controlling precipitation and dispersion conditions, and allowing the generation of well-defined and well-ordered nanorods and nanowires on various substrates. ZnO nanorods and nanowires have been prepared by the thermal decomposition of methenamine and zinc nitrate in aqueous solution at temperature of ~90°C. The diameter of the nanorods is controlled by changing the interfacial free energy chemically by changing the concentration of the precursors. Nanorods and nanowires of iron oxide have been prepared from an aqueous solution of ferric salts heated in a regular oven at 100°C for up to 24 h, followed by an additional heat treatment in air at ~390°C. The size of nanowires is adjusted by electrostatically controlling the interfacial free energy, which is obtained by controlling the pH and ionic strength.

Solvo-thermal synthesis

Solvo-thermal synthesis method is based on the solvo-thermal chemical reactions at elevated temperatures and pressures. Heath et al. pioneered the solvo-thermal synthesis of semiconductor nanowires [82]. They synthesized Ge nanowires with diameters ranging from 7 to 30 nm and lengths of up to 10 μm by reducing $GeCl_4$ and phenyl-$GeCl_3$ by sodium metal in an alkane-solvent, heated and pressurized at 275°C and 100 atmospheres. Various nanorods and nanowires such as SiC, $CdWO_4$, InAs, CdS, and CdSe were later synthesized later using the solvo-thermal method [83]. The products are often characterized by low yield, low purity and poor uniformity in size and morphology.

Solution–liquid–solid (SLS) growth

Analogous to VLS growth, semiconductor nanowires can also be synthesized in solution using metallic particles as growth seeds [84–86]. In this so called SLS growth mode, metallic droplets are formed on the substrate in the solution, and growth materials dissolve into the droplets at the solution–liquid interface. Semiconductor materials are precipitated from the droplets and form nanowires. Buhro et al. [84] reported on the growth of III–V semiconductor nanowires such as InP, InAs and GaAs, using the SLS mechanism, in which nanoparticles of low melting temperature metals or alloys such as In or Al_xGa_{1-x} alloys are used as catalysts and the organo-metallic reactions for nanowire growth are conducted at low temperatures of ~203°C in hydrocarbon solvents. Semiconductor polycrystalline fibres or near single crystal whiskers of InP, InAs, and GaAs, with diameters of 10–150 nm and lengths of up to several micrometers have been produced. For conventional and ambient-pressure solutions, metallic seed particles with eutectic temperatures exceeding the boiling temperature of the solvent can not be used.

Although nanowires can be grown using SLS with low melting point seed particles, at a temperature below the boiling point of conventional solvents, the quality and yield of the resulting nanowires are generally not sufficiently high for device applications.

Hanrath and Korgel [86] used organic-monolayer-protected metallic particles to grow semiconductor nanowires using SLS in pressurized supercritical solution at high temperature. Si and Ge nanowires have been grown using alkanethiol-capped gold nanocrystals in supercritical hexane with silicon (diphenylsilane) and germanium precursors at 500°C and 30 bar, and 375°C and 20 MPa, respectively. Bulk quantities of defect-free nanowires with diameters ranging from 4 to 30 nm and length of several micrometers have been obtained using this method.

Properties and applications of 1-D nanostructures

As the size of the nanostructures decrease, the energy spectrum or density of states (DOS) changes from a continuum of states into a discrete set of quantized states. The DOS is a strong function of the spatial dimensions. Figure 18 shows the variation of the DOS with changing quantization dimension. Many unique physical properties of nanowires can be related to their state spectrum and the appearance of discrete energy states and a sharp distribution of DOS as their size diminishes.

Electronic properties

Electron transport in nanowires has attracted a great deal of interest. In order to characterize the electronic properties of nanowires, a important first step is to align the nanowires on to patterned electrodes. Huang et al. [87] have reported an approach to align nanowires using fluid flows, with separation and spatial location, readily controlled. Parallel and crossed arrays of nanowires have been demonstrated with single and sequential crossed flows of fluid.

To characterize p–n, p–p, and n–n junctions, p- and n-type silicon nanowires have been dispersed in acetone and deposited sequentially on to an oxidized Si substrate. Contacts to the silicon nanowires were defined by electron beam lithography. Cui and Lieber have measured the electronic properties of those junctions and observed the current rectification of the junctions which is similar to bulk semiconductor junctions [88].

Optical properties

As an example of studies of the optical properties of nanowires, we discuss research on ZnSe nanowires. The work reported to date has been rather limited [89–92]. It has been found that it is particularly difficult to obtain perfectly stoichiometric ZnSe nanowires and unless the growth conditions are optimized to minimize the deviations from stoichiometry, the resulting nanowires contain too high a concentration of defects to be of use in light-emitting applications. Small deviations from stoichiometry can be detected only by very sensitive techniques and photoluminescence (PL) is one such technique. Most of the work on room temperature PL spectra of ZnSe nanowires shows that the spectrum consists of two characteristic emission peaks—the near band edge emission (NBE) at 463 nm (2.68 eV) [91] and a broad deep level (DL) emission at ~500–680 nm (1.8–2.48 eV) [93]. The DL emissions are usually associated with dislocations, stacking faults and non-stoichiometric defects [94–96]. The intensity of the NBE emission depends strongly on the growth method [91] and is much weaker than the DL emission. In some cases, the NBE emission is even absent [89, 92]. In Ref. 91, where the ZnSe nanowires were fabricated by MOCVD, it was shown that the intensity ratio of

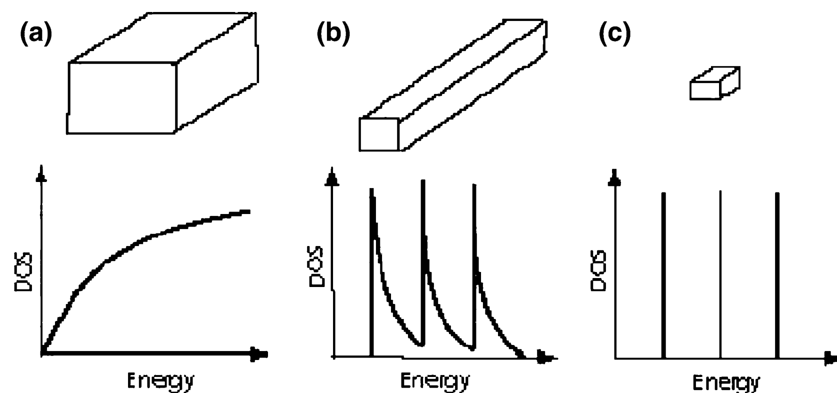

Fig. 18 A schematic illustration of the density of states (DOS) distribution in a bulk semiconductor (**a**), in a semiconductor nanowire (**b**) and a semiconductor quantum-dot (**c**): note that by forming a heterostructure within a one-dimensional (1-D) nanostructure (or nanowire), one can create a three dimensionally confined region (or quantum-dot)

the NBE to the DL emissions were strongly dependent on the pressure of growth. The maximum intensity ratio was found for an optimal pressure, but at this pressure the yield of nanowires was a minimum. Hence, it becomes imperative to look for methods where we can have good yield of nanowires with high optical quality. We were able to demonstrate that post-growth treatment of ZnSe nanowires permits one to obtain nanowires dominated by NBE emission as shown in Fig. 19.

Time-resolved terahertz (THz) spectroscopy can also be used to study the optical and transport properties of nanowires [97]. As an example, Fig. 20 shows the results from an optical pump—THz probe experiment on an array of GaAs nanowires (Fig. 20a). The optical pump beam was comprised of 400 nm, 100 fs laser pulses from a frequency-doubled Ti:sapphire amplifier laser system (running at a repetition rate of 1 kHz). The normalized negative differential transmission ($-\Delta T$) of the THz probe pulse as a function of delay time with respect to the pump pulse is shown in Fig. 20b, and is representative of the transient photoconductivity in the nanowires [97]. The decay time of the signal becomes longer at higher fluences, most likely due to trap-filling effects that increase the carrier relaxation times in the nanowires. The inset in Fig. 20b shows bi-exponential fits to the normalized transient signals of the form $-\Delta T = A_1 \exp(-t/\tau_1) + A_2 \exp(-t/\tau_2)$, where the initial fast decay time τ_1 varies from about 4 to 13 ps as the average pump power increases from 0.5 to 3 mW, with a corresponding increase in τ_2 from 50 to 180 ps. The fast decay time τ_1 could be due to initial trapping at surface states on the nanowires. Studies of the THz polarization anisotropy of the nanowires are currently underway.

Low dimensional laser structures

Arakawa et al. first proposed a new type of laser using low dimensional structures as an active layer [98]. The

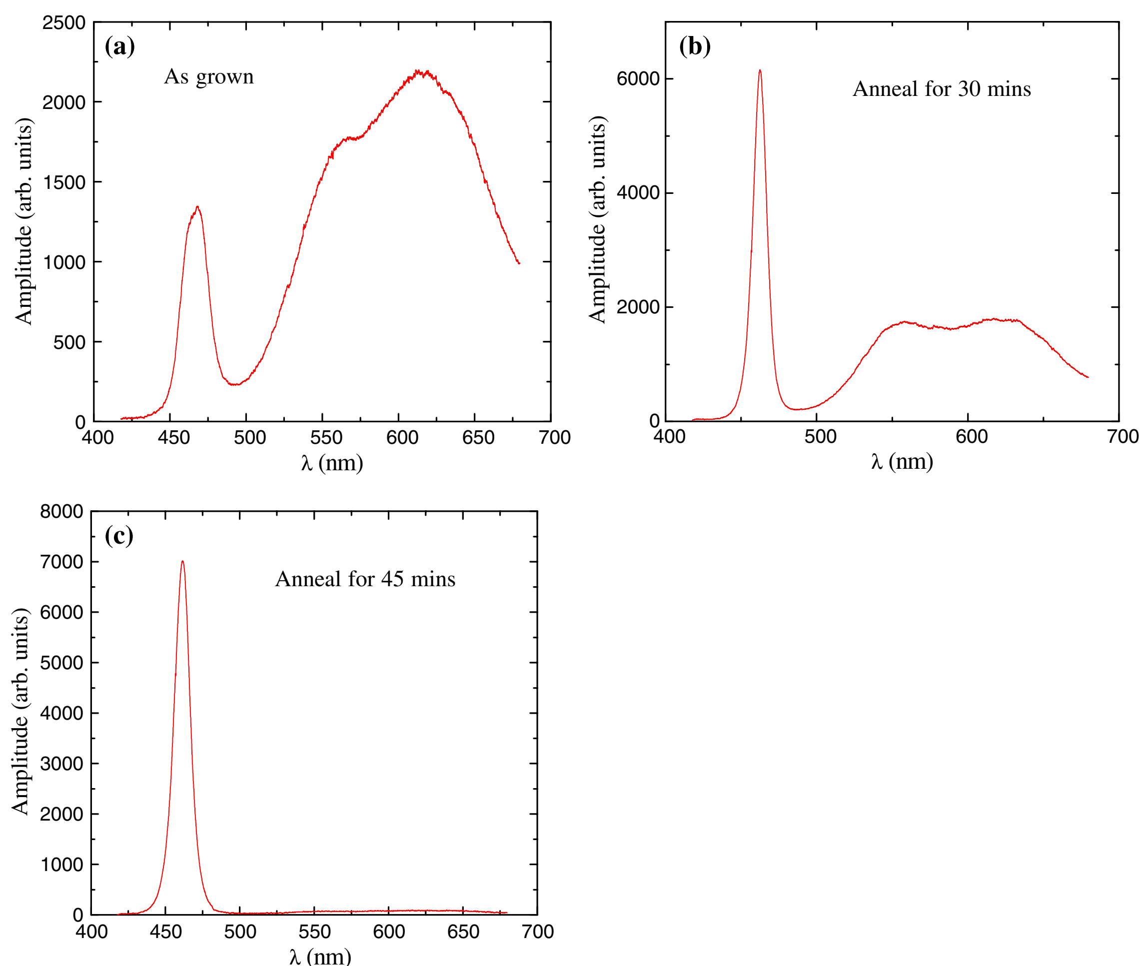

Fig. 19 Photoluminescence spectrum of ZnSe nanowires at room temperature: (**a**) as-grown nanowires, (**b**) after annealing in a Zn-rich atmosphere at 650°C for 30 min, and (**c**) after annealing in a Zn-rich atmosphere at 650°C for 45 min

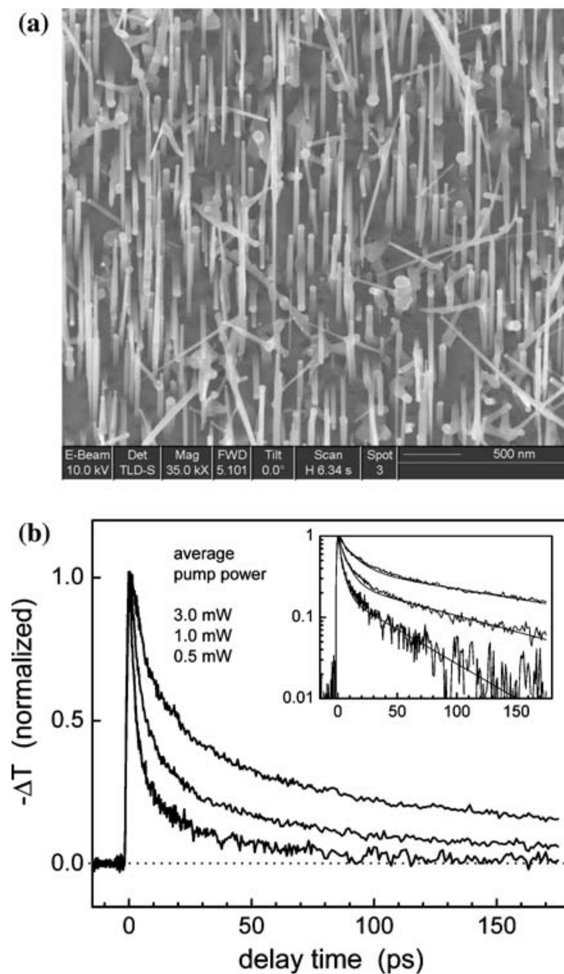

Fig. 20 Scanning electron microscope image of an array of GaAs nanowires (**a**), and associated optical pump—THz probe transient photoconductivity data in (**b**). The THz data in (**b**) shows the normalized change in transmission of the THz pulse through the sample as a function of delay time with respect to 400 nm, 100 fs pump pulses at various fluences. The inset is a semi-log plot of the same data showing bi-exponential fits to the decay dynamics, as discussed in the text

threshold current of the laser is predicted to be lower and less temperature sensitive. Asada et al. have theoretically studied the gain of the quantum-well, quantum-wire, and quantum-dot (QD) lasers [99]. They found that the shape of gain spectra become sharper with increasing quantization dimension and the peak gain increase with increasing quantization dimension.

Semiconductor nanowire lasers

Semiconductor nanowires form natural laser cavities. Nanowire nanolaser of wide band-gap semiconductor ZnO has been demonstrated by Yang et al. at room temperature in ultraviolet [100]. Lasing with sharp peak and rapid increase of intensity occurs as the excitation intensity exceeds a threshold of about 40 kW/cm^2. The lasing threshold is quite low as compared with reported values of about 300 kW/cm^2 for random lasing in disordered particles or thin films [101].

Lieber et al. have demonstrated electronically driven single-nanowire lasers [102]. A n-type CdS nanowire is assembled onto p-type Si electrodes to form a n-CdS/p-Si heterostructure. The n-type CdS nanowire forms the cavity of the laser. At low injection current, the emission spectrum shows a broad peak. Very sharp peaks emerge as the injection current exceeds the threshold current of about 200 μA.

An optical microcavity is an indispensable component that can provide the necessary feedback for the build-up of oscillations in a semiconductor laser. Normally, an optical cavity is formed by two end mirrors. A structure called a distributed Bragg reflector (DBR) has been used to enhance the end reflectivity of optical cavities in surface emitting lasers [103], where alternative high and low refractive index materials form a 1-D periodic structure called a DBR mirror, having high reflectivity for a selected wavelength. Alternatively, a mechanism called distributed feedback (DFB) [104, 105] has been widely used in semiconductor lasers, where a 1-D periodic structure is embedded to induce Bragg diffraction, resulting in a standing wave composed of two counter-propagating waves. The above two structures (i.e., DBR and DFB cavities) can be viewed as a 1-D photonic crystal cavity with the advent of the concept of photonic crystals (PCs)—these are artificial structures with a periodic spatial variation of dielectric constant [106, 107]. Owing to the occurrence of a full photonic band gap (where the light in all the directions can not propagate in the PCs), it is feasible to implement optical microcavities with intentionally introduced defects, similar to the concept of a DBR cavity, where the periodic structure surrounding the defect acts like DBR mirrors. Due to the small group velocity around the band edge [108, 109] and an effective total internal reflection (TIR) condition at the boundary, as analyzed in Ref. 8, microcavities operating around the band edge (without the introduction of defects) can have high-Q values, similar to the concept of a DFB cavity. Despite the similarity, PC microcavities can be extended to 2-D and 3-D, to yield confining and coupling mechanism unattainable in traditional 1-D structures.

We found that PCs consisting of semiconductor nanowire arrays grown by VLS are excellent candidates for photonic elements and devices, such as microcavities, due to the high dielectric constant contrast and high aspect ratio [110]. In addition, it is easy

to control the crystal structure by patterning the metal catalysis, and the versatility of composition modulation of nanowires (including II–VI, III–V, and ternary III–V) makes the integration of optical components in diversified wavelength ranges possible. Plane wave expansion (PWE) and finite difference time domain (FDTD) techniques allow one to study the optical properties of nanowire based PCs. It was found that arrays consisting of nanowires with radius at or below the edge of the effective single-wire confining range for a stand alone Fabry–Perot cavity can still form a high-Q value cavity with single mode operation. As shown in Fig. 21, the light is confined in the nanowire array both in the plane of periodicity and in the vertical direction. A 3-D FDTD calculation gives the Q value for the mode in a band edge cavity in Fig. 21a as 18,000 and for a defect cavity in Fig. 21b as 1800 [111]. The mode volume for the defect mode is about 1.7 $(\lambda/n)^3$.

The nanowire array based PC microcavity laser may extend state-of-art 1-D DBR and DFB lasers into 2-D ones with a working range from the ultraviolet to near infrared. In addition to microcavities, we are currently investigating the waveguide in the line defect of nanowire PCs and the propagation behavior in the pass bands. We found that around certain regions of the pass bands, it is possible to implement negative

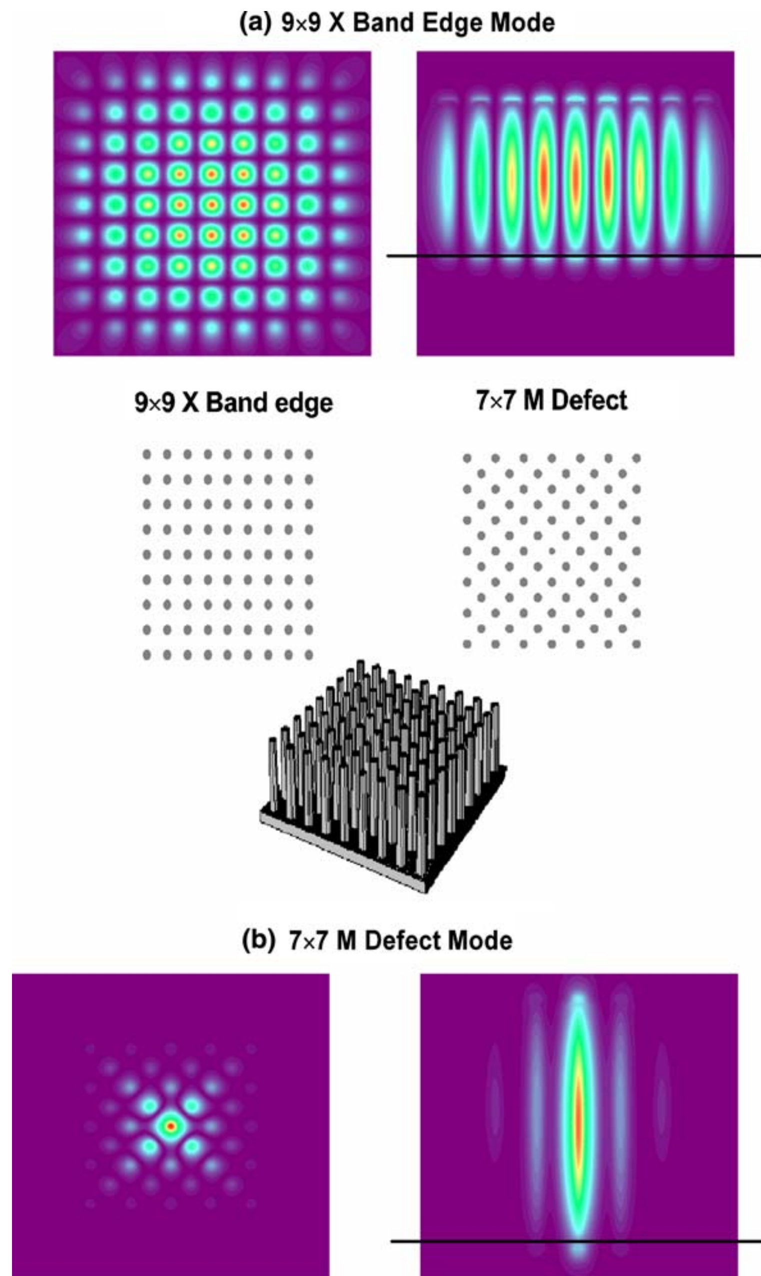

Fig. 21 Illustration of the space structures of nanowire array based photonic crystal cavities and the cross-section of the mode in these cavities as calculated using a 3D finite difference time domain calculation. The black lines shown in the vertical cross-section indicate the confinement in this direction (see Ref. 111)

refraction devices such as lenses with these nanowire arrays, which will be discussed in another paper. With these optical components, such as microlasers, waveguides, sharp benders, beam splitters and lens, nanowire array based PC may provide a platform for dense optical integration. Recently, III–V nanowires have been reported to epitaxially and vertically grow on silicon substrates [112]. On-chip dense optical integrated photonic circuits with nanowire array PCs may be realized on silicon substrates with this technique, which would be a promising method to enable the interconnection between silicon-based electronics and photonics.

Ultrashort optical pulse generation

Sources of ultrashort optical pulses are attractive for many photonic applications such as telecommunications, imaging, and sensing. Optical sources based on semiconductor materials offer attractive features such as compact size, low cost, and high efficiency. Using the technique of mode-locking, powerful short pulses with sub-picosecond durations can be obtained from semiconductor-based systems [113]. A key requirement of mode-locking for the generation of ultrashort pulses is a broad gain bandwidth. Asymmetric quantum-wells (QWs) can further broaden the gain bandwidth of a semiconductor laser structure which is desirable for applications that require broadband wavelength tuning. Figure 22 shows the conduction band profile of an InGaAs asymmetric QW active region that has been fabricated using molecular beam epitaxy. The InGaAs QWs have a thickness of 6 nm and transition

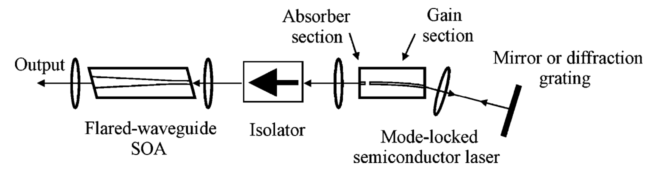

Fig. 23 External cavity mode-locked semiconductor oscillator coupled to a flared-waveguide Semiconductor optical amplifier (SOA). Adapted from [116] with permission

wavelengths of 965 and 995 nm. Mode-locking the semiconductor lasers in an external cavity has generated optical pulses with durations of 2.0–3.9 ps that can be tuned over 61 nm [114].

We also fabricated mode-locked QW diode lasers producing short picosecond pulses at a wavelength of 1080 nm [115]. The active region of these devices has been engineered to overlap with the gain region of a ytterbium-doped fibre. Semiconductor optical amplifiers (SOAs) with good performance have also been demonstrated in this wavelength range. Figure 23 depicts a schematic of the setup used for short pulse generation and amplification. A key feature of the SOA is that it contains a flared waveguide which improves gain saturation and energy extraction aspects of the amplifier. Pulses 5 ps in duration with a central wavelength of approximately 1080 nm have been amplified to an average power of 50 mW. The amplified pulses exhibit a frequency chirp that can be partially compensated using pulse compression techniques. A modified dual-grating compressor has been used to temporally reduce the amplified pulse width from 5 ps to 520 fs, yielding a pulse peak power of over 40 W. Figure 24 shows an intensity autocorrelation

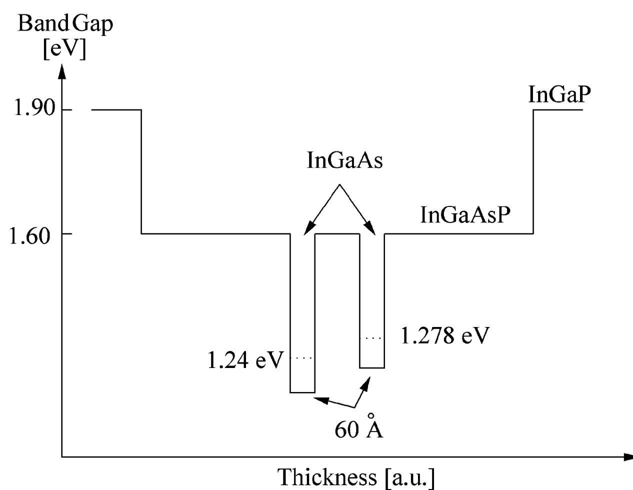

Fig. 22 Schematic illustration of the conduction band edge profile of the active region of a compositionally asymmetric quantum-well (QW) laser. Note: the thickness axis is not drawn to scale

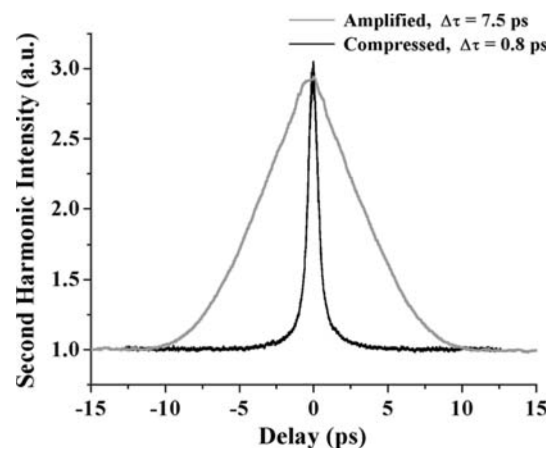

Fig. 24 Second order intensity autocorrelation traces of the amplified and compressed pulse. The quoted pulse widths in the figure are the FWHM of the autocorrelation trace. Assuming a hyperbolic-secant-squared pulse shape, the compressed pulse duration is 520 fs

trace of the pulse train following amplification and compression. The compressed pulses are still a factor of 2.5 above their Fourier transform limit, indicating the need for higher order dispersion compensation. Seeding a Yb:fibre amplifier with pulses from the diode laser oscillator, or oscillator and SOA combination, will provide powerful ultrashort pulses with variable repetition rate and excellent beam quality. This hybrid technology approach could prove of interest for a number of applications.

Research on mode-locked diode lasers in a number of laboratories has resulted in improved performance characteristics such as higher output power, shorter pulse duration, and enhanced beam quality. Innovative semiconductor waveguide structures [117] have resulted in record mode-locked peak powers as high as 1.4 kW from an all-semiconductor system [118]. Work has also progressed in the development of vertical external cavity mode-locked semiconductor lasers. Such devices are capable of delivering ultrashort pulses with excellent beam quality [119]. An area of research that has received much interest recently is that of nanostructured laser active regions. Novel laser structures containing quantum-wires and QDs can offer a number of potential advantages over QW designs. In particular, QD lasers have received considerable attention in terms of future perspectives [120]. Furthermore QD lasers exhibit features that are of interest for mode-locking applications, and a number of mode-locked lasers containing QD active regions have already been fabricated. Thompson et al. discuss the advantages in their report on a colliding pulse mode-locked QD semiconductor laser operating at a wavelength of 1.1 μm [121]. Kuntz et al. achieved Fourier-limited short picosecond pulses at 1.3 μm wavelength and a repetition rate of 50 GHz [122]. Finally, high power ultrashort pulses with a duration as short as 400 fs have been obtained by Rafailov et al. directly from a mode-locked two-section QD laser operating at 1260 nm [123]. It is clear that mode-locked semiconductor laser sources based on quantum-wire or QD materials show potential for deployment in a variety of linear and nonlinear photonic devices.

Photodetectors

The detection of long-wavelength (e.g., 10 μm) infrared radiation requires a semiconductor with small band gap (i.e., as low as 0.1 eV). HgCdTe is commonly used as the detector material due to its high responsibility. However, there are difficulties in epitaxial growth and processing of this II–VI semiconductor material resulting in low yield and ultimately high cost. Quantum wells are also used as infrared photodetector materials using intersubband optical transitions in quantum wells as the detection mechanism. However, the quantum efficiency of such quantum-well infrared photodetectors (QWIPs) is much lower than that of HgCdTe. QDs are also used for infrared photodetectors using optical transitions between bound states in the conduction/valence bands [113–118]. The potential advantages of QD infrared photodetectors are anticipated due to a reduction in the relaxation rates between the confined states leading to increased detection efficiency and increased sensitivity to normal incident photoexcitation as a result of breaking polarization selection rules. Nanowire photodetectors in ultraviolet have been demonstrated using ZnO nanowires as the detector material [119]. Individual ZnO nanowires are highly insulating in the dark with a resistivity above 3.5 MΩ cm. The nanowire resistivity decreases by 4–6 orders of magnitude when the nanowires are exposed to ultraviolet light.

Conclusions

In this article, the synthesis, properties and applications of nanowires were reviewed. Approaches to both the direct synthesis and also patterning were discussed with a view to forming both organized systems of nanowires, as well as random distributions of nanowires on substrates that can serve directly or indirectly as the basis for forming nanophotonic devices. We discussed a number of potential nanophotonic device opportunities including those in the emission and detection of light. We showed how unique opportunities can arise when one combines the ability to position and control the growth of high quality organized nanowire structures. An example of the latter was that of nanowire cavity structures possessing high Q and relatively small mode volume, suitable for efficient next generation laser systems. Clearly such 1-D nanostructures are highly promising for next generation nanophotonic devices and systems.

Acknowledgements The authors gratefully acknowledge financial support from CIPI and NSERC.

References

1. S. Dobrin, X. Lu, F.Y. Naumkin, J.C. Polanyi, J.S.Y. Yang, Surf. Sci. **573**(2), L363 (2004)
2. D.E. Brown, D.J. Moffat, R.A. Wolkow, Science **279**, 542 (1998)
3. S. Dobrin, K.R. Harikumar, J.C. Polanyi, Surf. Sci. **561**, 11 (2004)

4. E.P. Marsh, T.L. Gilton, W. Meier, M.R. Schneider, J.P. Cowin, Phys. Rev. Lett. **61**, 2725 (1988)
5. X.L. Zhou, J.M. White, Surf. Sci. **241**, 259 (1991)
6. St. J. Dixon-Warren, E.T. Jensen, J.C. Polanyi, J. Chem. Phys. **98**, 5938 (1993)
7. Q.Y. Yang, W.N. Schwarz, P.J. Lasky, S.C. Hood, N.L. Loo, R.M. Osgood Jr., Phys. Rev. Lett. **72**, 3068 (1994)
8. H. Xu, R. Yuro, I. Harrison, Surf. Sci. **411**, 303 (1998)
9. K.A. Khan, N. Camillone III, R.M. Osgood Jr., J. Phys. Chem. **B103**, 5530 (1999)
10. G.G. Totir, Y. Le, R.M. Osgood Jr., J. Phys. Chem. **B109**, 8452 (2005)
11. C.A. Schmuttenmaer, C.C. Miller, J.W. Herman, J. Cao, D.A. Mantell, Y. Gao, R.J.D. Miller, Chem. Phys. **205**, 91 (1996)
12. P. Petroff, A. Gossard, W. Wiegmann, Appl. Phys. Lett. **45**, 620 (1984)
13. T. Fukui, H. Saito, Appl. Phys. Lett. **50**, 824 (1987)
14. M. Miller, H. Weman, C. Pryor, M. Krishnamurthy, P. Petroff, H. Kroemer, L. Merz, Phys. Rev. Lett. **68**, 3464 (1992)
15. S. Hara, J. Ishizaki, J. Motohisa, T. Fukui, H. Hasegawa, J. Crystal Growth **145**, 692 (1994)
16. J. Ishizaki, S. Goto, M. Kishida, T. Fukui, H. Hasegawa, Jpn. J. Appl. Phys. **33**, 721 (1994)
17. F. Laruelle, F. Lelarge, Z. Wang, T. Mélin, A. Cavanna, B. Etienne, J. Crystal Growth **175/176**, 1087 (1997)
18. T. Kato, T. Takeuchi, Y. Inoue, S. Hasegawa, K. Inoue, H. Nakashima, Appl. Phys. Lett. **72**, 465 (1998)
19. T. Ota, K. Maehashi, J. Christen, K. Oto, K. Murase, H. Nakashima, Physica **E11**, 228 (2001)
20. S. Francoeur, A. Norman, A. Mascarenhas, E. Jones, J. Reno, S. Lee, D. Follstaedt, Appl. Phys. Lett. **81**, 529 (2002)
21. R. Nötzel, N. Ledentsov, L. Däweritz, K. Ploog, M. Hohenstein, Phys. Rev. **B45**, 3507 (1992)
22. H. Omi, T. Ogino, Appl. Phys. Lett. **71**, 2163 (1997)
23. W. Tsang, A. Cho, Appl. Phys. Lett. **30**, 293 (1997)
24. E. Kapon, M. Tamargo, D. Hwang, Appl. Phys. Lett. **50**, 347 (1987)
25. R. Bhat, E. Kapon, J. Werner, D. Hwang, N. Stoffel, M. Koza, Appl. Phys. Lett. **56**, 863 (1990)
26. S. Koshiba, H. Noge, H. Akiyama, T. Inoshita, Y. Nakamura, A. Shimizu, Y. Nagamune, M. Tsuchiya, H. Kano, H. Sakaki, K. Wada, Appl. Phys. Lett. **64**, 363 (1994)
27. S. Simhony, E. Kapon, E. Colas, D.M. Hwang, N. Stoffel, P. Worland, Appl. Phys. Lett. **59**, 2225 (1991)
28. W. Tribe, M.J. Steer, D. Mowbray, M. Skolnick, A. Forshaw, J. Roberts, G. Hill, M. Pate, C. Whitehouse, G. Williams, Appl. Phys. Lett. **70**, 993 (1997)
29. W. Tribe, M. Steer, A. Forshaw, K. Schumacher, D. Mowbray, D. Whittaker, M. Skolnick, J. Roberts, G. Hill, Appl. Phys. Lett. **73**, 3420 (1998)
30. E. Kapon, F. Reinhardt, G. Biasiol, A. Gustafsson, Appl. Surf. Sci. **123/124**, 674 (1998)
31. M. Steer, D. Mowbray, M. Skolnick, W. Tribe, A. Forshaw, D. Whittaker, J. Roberts, A. Cullis, G. Hill, M. Pate, C. Whitehouse, Physica **E2**, 949 (1998)
32. R. Nötzel, M. Ramsteiner, J. Menniger, A. Trampert, H. Schönherr, L. Däweritz, K. Ploog, J. Appl. Phys. **80**, 4108 (1996)
33. K. Robbie, M.J. Brett, J. Vac. Sci. Technol. **A15**, 1460 (1997)
34. K. Robbie, G. Beydaghyan, T. Brown, C. Dean, J. Adams, C. Buzea, Rev. Sci. Instr. **75**, 1089 (2004)
35. K. Kaminska, T. Brown, G. Beydaghyan, K. Robbie, Appl. Opt. **42**, 4212 (2003)
36. K. Kaminska, M. Suzuki, K. Kimura, Y. Taga, K. Robbie, J. Appl. Phys. **95**, 3055 (2004)
37. M.O. Jensen, M.J. Brett, Opt. Expr. **13**, 3348 (2005)
38. K. Kaminska, K. Robbie, Appl. Opt. **43**, 1570 (2004)
39. T. Karabacak, J.P. Singh, Y.P. Zhao, G.C. Wang, T. Lu, Phys. Rev. **B68**, 125,408 (2003)
40. C. Buzea, G. Beydaghyan, C. Elliott, K. Robbie, Nanotechnol. **16**, 1986 (2005)
41. G. Beydaghyan, K. Kaminska, T. Brown, K. Robbie, Appl. Opt. **43**, 5343 (2004)
42. K. Robbie, M.J. Brett, D.J. Broer, Nature **399**, 764 (1999)
43. K.E. Gilbertson, W.H. Finlay, C.F. Lange, M.J. Brett, D. Vick, Y.S. Cheng, Aerosol. Sci. **36**, 933 (2005)
44. I. Hodgkinson, Q.H. Wu, M. Arnold, L. De Silva, G. Beydaghyan, K. Kaminska, K. Robbie, Appl. Opt. **45**, 1563 (2006)
45. C. Buzea, K. Robbie, K. Kaminska, G. Beydaghyan, T. Brown, C. Elliott, C. Dean, J. Vac. Sci. Technol. **B23**, 2545 (2005)
46. K. Kaminska, A. Amassian, L. Martinu, K. Robbie, J. Appl. Phys. **97**, 013511–1 (2005)
47. A.L. Barabasi, H.E. Stanley, *Fractal Concepts in Surface Growth* (Cambridge University Press, 1995)
48. R. Wagner, W. Ellis, Appl. Phys. Lett. **4**, 89 (1964)
49. R. Finkelman, R. Larson, E. Dwornik, J. Crystal Growth, **22**, 159 (1974)
50. E. Givargizov, J. Crystal Growth **31**, 20 (1975)
51. G. Bootsma, H. Gassen, J. Crystal Growth **10**, 223 (1971)
52. E. Givargizov, J. Crystal Growth **20**, 217 (1973)
53. J. Weyher, Mater. Sci. Eng. **20**, 171 (1975)
54. J. Weyher, M. Surowiec, J. Crystal Growth **43**, 245 (1978)
55. J. Weyher, J. Crystal Growth **43**, 235 (1978)
56. J. Westwater, D. Gosain, S. Tomiya, S. Usui, H. Ruda, J. Vac. Sci. Technol. **B15**, 554 (1997)
57. K. Hiruma, M. Yazawa, K. Haraguchi, K. Ogawa, J. Appl. Phys. **74**, 3162 (1993)
58. K. Hiruma, M. Yazawa, T. Katsuyama, K. Ogawa, M. Koguchi, H. Kakibayashi, J. Appl. Phys. **77**, 447 (1995)
59. A. Viswanath, K. Hiruma, T. Katsuyama, Superlat. Microstruct. **14**, 105 (1993)
60. B. Ohlsson, M. Björk, M. Magnusson, K. Deppert, L. Samuelson, L. Wallenberg, Appl. Phys. Lett. **79**, 3335 (2001)
61. A. Morales, C. Lieber, Science **279**, 208 (1998)
62. J. Hu, T. Odom, C. Lieber, Acc. Chem. Res. **32**, 435 (1999)
63. X. Duan, C. Lieber, Adv. Mater. **12**, 298 (2000)
64. X. Duan, J. Wang, C. Lieber, Appl. Phys. Lett. **76**, 1116 (2000)
65. Z. Wu, X. Mei, D. Kim, M. Blumin, H. Ruda, Appl. Phys. Lett. **81**, 5177 (2002)
66. Z. Wu, X. Mei, D. Kim, M. Blumin, H. Ruda, J. Liu, K. Kavanagh, Appl. Phys. Lett. **83**, 3368 (2003)
67. Y. Cui, L. Lauhon, M. Gudiksen, J. Wang, C. Lieber, Appl. Phys. Lett. **78**, 2214 (2001)
68. T. Shimada, K. Hiruma, M. Shirai, M. Yazawa, K. Haraguchi, T. Sato, M. Matsui, T. Katsuyama, Superlat. Microstruct. **24**, 453 (1998)
69. M. Gudiksen, L. Lauhon, J. Wang, D. Smith, C. Lieber, Nature **415**, 617 (2002)
70. T. Sato, K. Hiruma, M. Shirai, K. Tominaga, K. Haraguchi, T. Katsuyama, T. Shimada, Appl. Phys. Lett. **66**, 159 (1995)
71. K. Haraguchi, K. Hiruma, T. Katsuyama, K. Tominaga, M. Shirai, T. Shimada, Appl. Phys. Lett. **69**, 386 (1996)
72. K. Haraguchi, K. Hiruma, K. Hosomi, M. Shirai, T. Katsuyama, J. Vac. Sci. Technol. **B15**, 1685 (1997)

73. Y. Cui, X. Duan, J. Hu, C. Lieber, Phys. Chem. **104**, 5213 (2000)
74. K. Haraguchi, T. Katsuyama, K. Hiruma, K. Ogawa, Appl. Phys. Lett. **60**, 745 (1992)
75. M. Björk, B. Ohlsson, T. Sass, A. Persson, C. Thelander, M. Magnusson, K. Deppert, L. Wallenberg, L. Samuelson, Appl. Phys. Lett. **80**, 1058 (2002)
76. Y. Wu, R. Fan, P. Yang, Nano Lett. **2**, 83 (2002)
77. L. Lauhon, M. Gudiksen, D. Wang, C. Lieber, Nature **420**, 57 (2002)
78. J. Goldberger, R. He, Y. Zhang, S. Lee, H. Yan, H. Choi, P. Yang, Nature **422**, 599 (2003)
79. L. Vayssieres, N. Beermann, S. Lindquist, A. Hagfeldt, Chem. Mater. **13**, 233 (2001)
80. L. Vayssieres, K. Keis, A. Hagfeldt, S. Lindquist, Chem. Mater. **13**, 4395 (2001)
81. L. Vayssieres, Adv. Mater. **15**, 464 (2003)
82. J. Heath, F. LeGoues, Chem. Phys. Lett. **208**, 263 (1993)
83. K. Tang, Y. Qian, J. Zeng, X. Yang, Adv. Mater. **15**, 448 (2003)
84. T. Trentler, K. Hickman, S. Goel, A. Viano, P. Gibbons, W. Buhro, Science **270**, 1791 (1995)
85. H. Yu, W. Buhro, Adv. Mater. **15**, 416 (2003)
86. T. Hanrath, B. Korgel, Adv. Mater. **15**, 437 (2003)
87. Y. Huang, X. Duan, Q. Wei, C. Lieber, Science **291**, 630 (2001)
88. Y. Cui, C. Lieber, Science **291**, 851 (2001)
89. Y. Zhu, Y. Bando, Chem. Phys. Lett. **377**, 367 (2003)
90. X.T. Zhang, K.M. Ip, Z. Liu, Y.P. Leung, Q. Li, S.K. Hark, Appl. Phys. Lett. **84**, 2641 (2004)
91. X.T. Zhang, K.M. Ip, Z. Liu, Y.P. Leung, Q. Li, S.K. Hark, J. Appl. Phys. **95**, 5752 (2004)
92. B. Xiang, H.Z. Zhang, G.H. Li, F.H. Yang, F.H. Su, R.M. Wang, J. Xu, G.W. Lu, X.C. Sun, Q. Zhao, D.P. Yu, Appl. Phys. Lett. **82**, 3330 (2003)
93. S. Fujita, H. Mimoto, T. Naguchi, J. Appl. Phys. **50**, 1079 (1979)
94. X.B. Zhang, K.L. Ha, S.K. Hark, Appl. Phys. Lett. **79**, 1127 (2001)
95. V.P. Makhnii, I.V. Tkachenko, J. Opt. Technol. **70**(9), 665 (2003)
96. K.M. Ip, Z. Liu, C.M. Ng, S.K. Hark, Nanotechnology **16**, 1144 (2005)
97. D.G. Cooke, F.A. Hegmann, Y.I. Mazur, W.Q. Ma, X. Wang, Z.M. Wang, G.J. Salamo, M. Xiao, T.D. Mishima, M.B. Johnson, Appl. Phys. Lett. **85**, 3839 (2004)
98. Y. Arakawa, H. Sakaki, Appl. Phys. Lett. **40**, 939 (1982)
99. M. Asada, Y. Miyamoto, Y. Suematsu, IEEE J. Quantum Electron. **QE-22**, 1915 (1986)
100. M. Huang, S. Mao, H. Feick, H. Yan, Y. Wu, H. Kind, E. Weber, R. Russo, P. Yang, Science **292**, 1897 (2001)
101. H. Cao, J. Xu, D. Zhang, S. Chang, S. Ho, E. Seelig, X. Liu, R. Chang, Phys. Rev. Lett. **84**, 5584 (2000)
102. X. Duan, Y. Huang, R. Agarwal, C. Lieber, Nature **421**, 241 (2003)
103. T. Baba, T. Hamano, F. Koyama, K. Iga, IEEE J. Quant. Electron. **27**, 1347 (1991)
104. H. Kogelnik, C. Shank, Appl. Phys. Lett. **18**, 152 (1971)
105. I.P. Kaminow, H.P. Weber, E.A. Chandross, Appl. Phys. Lett. **18**, 497 (1971)
106. S. John, Phys. Rev. Lett. **58**, 2486 (1987)
107. E. Yablonovitch, Phys. Rev. Lett. **58**, 2059 (1987)
108. J.P. Dowling, M. Scalora, M.J. Bloemer, C.M. Bowden, J. Appl. Phys. **75**, 1896 (1994)
109. K. Sakoda, K. Ohtaka, T. Ueta, Opt. Express **4**, 481 (1999)
110. T. Xu, S. Yang, S.V. Nair, H.E. Ruda, Phys. Rev. **B72**, 045,126 (2005)
111. T. Xu, S. Yang, S.V. Nair, H.E. Ruda, Proc. SPIE **5971**, 262 (2005)
112. T. Martensson, C.P.T. Svensson, B.A. Wacaser, M.W. Larsson, W. Seifert, K. Deppert, A. Gustafsson, L.R. Wallenberg, L. Samuelson, Nano Lett. **4**, 1987 (2004)
113. P. Vasil'ev, *Ultrafast Diode Lasers* (Artech House Norwood, MA, 1995)
114. M.J. Brennan, J.N. Milgram, P. Mascher, H.K. Haugen, Appl. Phys. Lett. **81**, 2502 (2002)
115. M.J. Brennan, A.J. Budz, B.J. Robinson, P. Mascher, H.K. Haugen, IEEE Photon. Technol. Lett. **16**, 1798 (2004)
116. A.J. Budz, M.J. Brennan, H.K. Haugen, *Conference on Lasers and Electro-optics* (San Francisco, CA, 2004), paper CTuP6
117. S. Gee, G. Alphonse, J. Connolly, P.J. Delfyett, IEEE J. Select. Topics Quantum Electron, **4**, 209 (1998)
118. K. Kim, S. Lee, P.J. Delfyett, Opt. Express, **13**, 4600 (2005)
119. S. Hoogland, A. Garnache, I. Sagnes, J.S. Roberts, A.C. Tropper, IEEE Photon. Technol. Lett. **17**, 267 (2005)
120. D. Bimberg, J. Phys. D: Appl. Phys. **38**, 2055 (2005)
121. M.G. Thompson et al Electron. Lett. **41**, 248 (2005)
122. M. Kuntz et al New J. Phys. **6**, 181 (2004)
123. E.U. Rafailov et al Appl. Phys. Lett. **87**, 081,107 (2005)
124. S. Komiyama, O. Astafiev, V. Antonov, T. Kutsuwa, H. Hirai, Nature **403**, 405 (2000)
125. A. Yakimov, A. Dvurechenskii, A. Nikiforov, Y. Proskuryakov, J. Appl. Phys. **89**, 5676 (2001)
126. J. Phillips, J. Appl. Phys. **91**, 4590 (2002)
127. S. Tong, J. Liu, J. Wan, K. Wang, Appl. Phys. Lett. **80**, 1189 (2002)
128. D. Kuo, Y. Chang, Phys. Rev. **B67**, 353,131 (2003)
129. H. Kind, H. Yan, B. Messer, M. Law, P. Yang, Adv. Mater. **14**, 158 (2002)